The First High-contrast Images of Near High-mass X-Ray Binaries with Keck/NIRC2

M. Prasow-Émond[1,2,3] , J. Hlavacek-Larrondo[2] , K. Fogarty[4,5] , É. Artigau[3] , D. Mawet[4,6] , P. Gandhi[7] , J. F. Steiner[8] ,
J. Rameau[3,9] , D. Lafrenière[2,3] , A. Fabian[10] , D. J. Walton[11] , R. Doyon[2,3] , and B. B. Ren (任彬)[4,9,12,13,14]

[1] Department of Earth Science and Engineering, Imperial College London, Prince Consort Road, London SW7 2BP, UK; m.prasow-emond22@imperial.ac.uk
[2] Département de Physique, Université de Montréal, C.P. 6128, Succ. Centre-Ville, Montréal, QC H3C 3J7, Canada
[3] Trottier Institute for Research on Exoplanets, Université de Montréal, Département de Physique, C.P. 6128 Succ. Centre-ville, Montréal, QC H3C 3J7, Canada
[4] Division of Physics, Math, and Astronomy, California Institute of Technology, Pasadena, CA 91125, USA
[5] NASA Ames Research Center, Moffett Field, CA 94035, USA
[6] Jet Propulsion Laboratory, California Institute of Technology, Pasadena, CA 91109, USA
[7] Department of Physics and Astronomy, University of Southampton, Highfield, Southampton, SO17 1BJ, UK
[8] Center for Astrophysics | Harvard & Smithsonian, Cambridge, MA 02138, USA
[9] Univ. Grenoble Alpes, CNRS, IPAG, F-38000 Grenoble, France
[10] Institute of Astronomy, Cambridge University, Madingley Road, Cambridge CB3 0HA, UK
[11] Centre for Astrophysics Research, University of Hertfordshire, College Lane, Hatfield AL10 9AB, UK
[12] Université Côte d'Azur, Observatoire de la Côte d'Azur, CNRS, Laboratoire Lagrange, Bd de l'Observatoire, CS 34229, 06304 Nice cedex 4, France
[13] Department of Physics and Astronomy, The Johns Hopkins University, 3701 San Martin Drive, Baltimore, MD 21218, USA
[14] Department of Applied Mathematics and Statistics, The Johns Hopkins University, 3400 N Charles Street, Baltimore, MD 21218, USA

Abstract

Although the study of X-ray binaries has led to major breakthroughs in high-energy astrophysics, their circumbinary environment at scales of $\sim$100–10,000 au has not been thoroughly investigated. In this paper, we undertake a novel and exploratory study by employing direct and high-contrast imaging techniques on a sample of X-ray binaries, using adaptive optics and the vortex coronagraph on Keck/NIRC2. High-contrast imaging opens up the possibility to search for exoplanets, brown dwarfs, circumbinary companion stars, and protoplanetary disks in these extreme systems. Here we present the first near-infrared high-contrast images of 13 high-mass X-ray binaries located within $\sim$2–3 kpc. The key results of this campaign involve the discovery of several candidate circumbinary companions ranging from substellar (brown dwarf) to stellar masses. By conducting an analysis based on Galactic population models, we discriminate sources that are likely background/foreground stars and isolate those that have a high probability ($\gtrsim$60%–99%) of being gravitationally bound to the X-ray binary. This paper seeks to establish a preliminary catalog for future analyses of proper motion and subsequent observations. With our preliminary results, we calculate the first estimate of the companion frequency and the multiplicity frequency for X-ray binaries: $\approx$0.6 and 1.8 ± 0.9, respectively, considering only the sources that are most likely bound to the X-ray binary. In addition to extending our comprehension of how brown dwarfs and stars can form and survive in such extreme systems, our study opens a new window to our understanding of the formation of X-ray binaries.

Unified Astronomy Thesaurus concepts: Multiple stars (1081); X-ray binary stars (1811); Near infrared astronomy (1093); High mass x-ray binary stars (733); Coronagraphic imaging (313); High contrast techniques (2369); Direct imaging (387); Exoplanet detection methods (489); Substellar companion stars (1648)

1. Introduction

X-ray binaries are semidetached binary systems in which a compact object (white dwarf (WD), neutron star (NS), or stellar-mass black hole (BH)) accretes material from a donor star. These systems undergo several extreme physical phenomena, such as processes acting predominantly in soft X-rays (e.g., Khargharia et al. 2010; Tetarenko et al. 2021) and detectable X-ray pulsations (e.g., Lutovinov et al. 2005).

The variations in physical processes among different X-ray binaries are directly linked to the mass of the donor star. Over 90% of these systems can be classified into two distinct categories: high-mass X-ray binaries (HMXBs; $M_{\rm donor} \gtrsim 8\,M_\odot$) and low-mass X-ray binaries (LMXBs; $M_{\rm donor} \lesssim 1, 5\,M_\odot$; e.g., Tauris & van den Heuvel 2006). LMXBs are relatively old systems ($>10^9$ yr) harboring a K–M spectral type donor star, where the process of mass transfer is believed to be triggered by

Roche lobe overflow (RLO; e.g., Savonije 1978). RLO is triggered either by stellar evolution or by angular momentum loss (e.g., Paczyński 1967; Verbunt & Zwaan 1981; Strohmayer 2002; Justham et al. 2006; Chen & Podsiadlowski 2016; Seto 2018; Van et al. 2019). The transferred mass then agglomerates to form an accretion disk around the compact object, giving rise to transient accretion and X-ray emission (e.g., Charles & Coe 2006).

As for HMXBs, they are generally thought to be younger systems ($\lesssim 10^7$ yr) harboring a massive O–B spectral type donor star. The transferred and accreted matter is thought to predominantly come from the capture of a fraction of the stellar winds ejected from the donor star (e.g., Mohamed & Podsiadlowski 2007; Abate et al. 2013; El Mellah et al. 2019). There are two subcategories of HMXBs relevant to this work. First, we emphasize Be/X-ray binaries (BeXRBs), wherein the donor star is a fast-rotating Be star. In these systems, the X-ray emission is mainly triggered by the compact object passing through a diffuse and gaseous circumstellar disk surrounding the Be star (known as a decretion disk; e.g., Okazaki et al. 2002; Martin et al. 2011; Rímulo et al. 2018; Kravtsov et al. 2020).

Second, we highlight supergiant fast X-ray transients (SFXTs; Negueruela et al. 2006), characterized by the presence of a supergiant donor star and by fast transient X-ray flaring activity within the system (likely induced by an NS; e.g., Sidoli 2012; Ducci et al. 2019).

X-ray binaries are important touchstone objects for high-energy phenomena in astrophysics. They have been widely used to study several high-energy astronomical phenomena, including accretion physics (e.g., Done et al. 2007; Kara et al. 2019) and outflow/jet processes (e.g., Markoff et al. 2001; Fender et al. 2004; Mooley et al. 2018). However, the immediate surroundings of X-ray binaries, at the scale of ∼100–10,000 astronomical units (au), have been poorly studied. This paper undertakes a pioneering exploration of the circumstellar environments of X-ray binaries through the application of adaptive optics (AO) and direct/high-contrast imaging techniques. The goal is to probe a variety of phenomena, ranging from protoplanetary disks to debris disks and fallback disks, and particularly to search for wide-orbiting circumbinary companions (CBCs)—be they exoplanets, brown dwarfs, or stars.

Considering the discovery of planetary-mass CBCs orbiting both binary systems (e.g., Bakos et al. 2007; Desidera & Barbieri 2007; Eriksson et al. 2020) and compact objects (WDs or pulsars; e.g., Wolszczan & Frail 1992; Sigurdsson et al. 2003; Spiewak et al. 2018; Vanderburg et al. 2020; Blackman et al. 2021), it is not unfounded to expect CBCs orbiting X-ray binaries. A recent study argued that X-ray binaries could host planetary systems in close orbits detectable via X-ray eclipses (Imara & Di Stefano 2018). In this paper, we explore wider orbits (∼100–10,000 au), as the increased number of interactions within the system could lead to the ejection of potential CBCs from the direct environment of the X-ray binary (e.g., Bonavita et al. 2016).

In Prasow-Émond et al. (2022), we presented the first set of observations from a pilot study aiming to survey all X-ray binaries amenable for direct imaging within ∼3 kpc. We first targeted a γ Cassiopeiae−like X-ray binary harboring a Be donor star, RX J1744.7−2713, for which we had observations from two different bands and two epochs. We unveiled the presence of three potential CBCs within this system, exhibiting a strong likelihood of being stellar-mass CBCs. Here we present the first L'-band high-contrast images of 13 other systems and conduct a preliminary statistical analysis derived from the results of the first epochs of observations.

The paper is organized as follows: Section 2 presents the sample and how it was constructed. Section 3 presents the near-infrared observations and the data reduction and processing. Section 5 presents the first high-contrast images of the observed X-ray binaries. In Section 6, we analyze the images and explore the nature of the detection. Finally, in Section 7, we discuss our results and their implications.

2. The Sample

Despite the ongoing active search for new X-ray binaries both within and beyond our Galaxy (e.g., Gandhi et al. 2022), their presence remains relatively scarce. Our Galaxy hosts ∼300 identified X-ray binaries known to date (Liu et al. 2006, 2007). We drew on this list of X-ray binaries as our initial data set; however, not all of these systems are suitable for direct imaging with Keck/NIRC2. In order to build a sample of X-ray binaries that would yield optimal statistical constraints and mitigate potential biases, we used four selection criteria:

1. *Distance.* The system must be close enough to resolve the direct environment at ∼100–10,000 au scales. We chose a distance limit of ∼3 kpc within our Galaxy, which enables the detection of structures and objects located within a couple of thousands of au from the X-ray binary. The outer limit (10,000 au) corresponds to the approximate limit of the Keck/NIRC2 field of view (FOV).
2. *Brightness and Adaptive Optics.* The donor star must be bright enough ($I < 9$–10 mag) for the AO loop to be closed.
3. *Age.* We targeted young (≲100 Myr) X-ray binaries to favor the detection of substellar CBCs, considering the steep decline in planet brightness with time (e.g., Burrows et al. 2001). This limited us to bright LMXBs and HMXBs with a massive O/B donor star.
4. *Visibility.* We selected X-ray binaries visible from the W. M. Keck Observatory at the time of our observations (Keck Observatory Semesters 2017B and 2020A).

Applying these criteria narrowed down the initial list from ∼300 X-ray binaries to 19, out of which 14 were observed between 2017 and 2020 using Keck/NIRC2 (see Section 3.1 for more details). Our sample includes both HMXBs and LMXBs (e.g., MAXI J1820+070, V404 Cyg, 1A 0620–00); however, we have only observed HMXBs to date owing to observational constraints. Note that X-ray binary surveys are far from complete, as X-ray binaries can be undetectable in quiescence (e.g., Bird et al. 2007; Belczynski & Ziolkowski 2009). New X-ray binaries have also been discovered since we did our sampling (Avakyan et al. 2023; Neumann et al. 2023). Nonetheless, we assume that our sample is as complete as possible and that our results accurately represent the known population of X-ray binaries.

Figure 1 displays the position of the 14 observed targets onto the sky (Aitoff projection). It also indicates the distance from the observer (in kpc) and, if known, the nature of the system's compact object. In Section 4, we present a brief literature review for each of the observed X-ray binaries. Table 1 summarizes the known relevant physical properties of the systems, namely the X-ray binary type, X-ray emission class, donor star spectral type, and compact object type. Additional relevant physical properties can be found in the Appendix (see Table 5).

3. Observations and Data Reduction

3.1. Keck/NIRC2 Observations

On 2017 September 8, we observed four HMXBs from our survey sample using the Keck/NIRC2 vortex coronagraph (Mawet et al. 2005; Serabyn et al. 2016) in pupil-tracking mode in L' band ($\lambda = 3.776\ \mu m$, $\Delta\lambda = 0.700\ \mu m$; PI: Mawet), and with the narrow camera (plate scale of 9.971 ± 0.004 mas pixel^{-1}; Service et al. 2016). On 2018 January 3, we observed three additional HMXBs using a similar setting. Due to the successful and promising preliminary results of this initial campaign, we were awarded three supplementary nights of observation on 2020 July 11, 12, and 13 (PI: Fogarty). On the first night, we observed one additional target and reobserved two targets (RX J1744.7−2713 and γ Cas) using a similar setting. However, due to saturation, we had to downscale the frame size of γ Cas from 1024×1024 pixel^2 to 512×512 pixel^2. On 2020 July 12, we obtained data for three other HMXBs in L' band, in addition to reobserving RX J1744.7−2713 in K_s band ($\lambda = 2.146\ \mu m$, $\Delta\lambda = 0.311\ \mu m$). Finally, on 2020 July 13, we
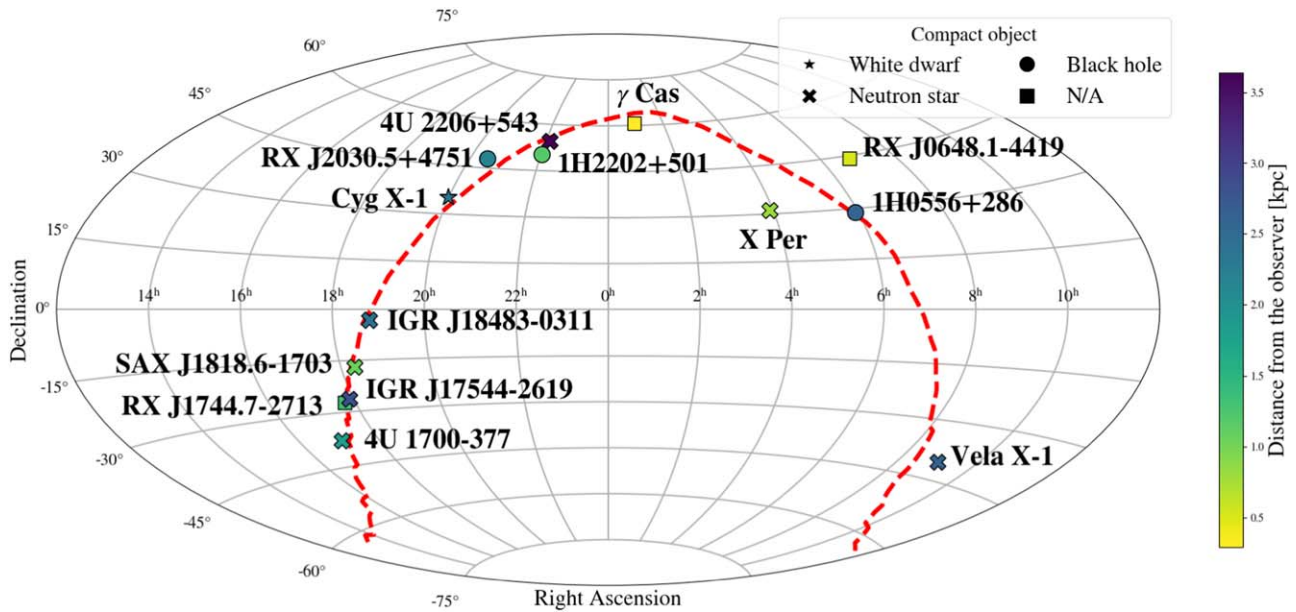
Figure 1. Position of the 14 observed X-ray binaries on the sky with equatorial coordinates and Aitoff projection, color-coded with distance from the observer in kpc. The nature of the compact object is illustrated with different markers: squares for WDs, crosses for NSs, asterisks for BHs, and circles for cases where the nature is either unavailable or uncertain. The red dotted line shows the approximate coordinates of the Galactic plane.

obtained data for three other HMXBs, totaling observations for 14 out of the 19 X-ray binaries in the sample.

During the observations, we used the Quadrant Analysis of Coronagraphic Images for Tip-tilt Sensing (Huby et al. 2017) to make tip-tilt adjustments to maintain precise centering of the target on the vortex focal plane mask. The observations were AO assisted using the Shack–Hartmann wave front sensor (which performs wave front sensing in R band) in 2017, in 2018, and on the last night of 2020. For the first two nights of our 2020 observations, we opted for the Pyramid wave front sensor instead. It performs wave front sensing in H (Wizinowich et al. 2000; Bond et al. 2018), which is more advantageous for the redder targets in our sample.

A summary of the observing log is presented in Table 2.

3.2. Data Reduction

Similarly to Prasow-Émond et al. (2022), we performed data reduction using the Vortex Image Processing (VIP) and NIRC2 Preprocessing packages (Gomez Gonzalez et al. 2017). To obtain a preprocessed data cube, we proceeded as follows: (1) flat-fielding of the frames, (2) bad pixel masking using the dark frames, (3) determination of the vortex center for each frame followed by cropping the science cube around the mean center, (4) removal of sky contribution via a principal component analysis (PCA) based technique, and (5) image registration to align the quasi-static speckle pattern across frames.

After acquiring the preprocessed data cube, we applied a PCA-based angular differential imaging (ADI; Marois et al. 2006) algorithm to obtain high-contrast images. Subsequently, we generated several images using two algorithms in VIP (annular PCA and full-frame PCA) for a broad range of principal components (from 1 to 50). This was done to ensure consistency in the detection of sources within the images (i.e., that the source was detected regardless of the number of principal components). We then listed sources with a signal-to-noise ratio (S/N) greater than 5 (or with a signal exceeding 4σ)

and determined the optimal number of principal components (n_{comp}) that maximized the S/N for each source.

3.3. Source Magnitude Calculation

To calculate the apparent and absolute magnitudes of the detected sources, we proceeded as follows: (1) We fit a 2D Gaussian profile to the point-spread function (PSF) cube to obtain the FWHM in milliarcseconds (mas) and to recenter the PSF frames. (2) The PSF cube was reduced into a single 2D PSF by computing the median of the frames. (3) We normalized the PSF so that the flux within a radius of 1 FWHM equated to 1. (4) Given a thermal artifact affecting the quality of the real PSF in our 2020 observations (as discussed in Prasow-Émond et al. 2022), we generated a normalized synthetic 2D PSF using the FWHM. (5) From the list of sources with S/N > 5, we generated a list of approximate coordinates using ds9. (6) Using the preprocessed cube, the optimal number of principal components, and the approximate coordinates, we fit the astrometric parameters (θ, the position angle in degrees, and ρ, the relative separation from the X-ray binary in pixels) and photometric parameters (f_1, the number of counts within an aperture radius of 3 FWHM, i.e., the relative flux) using a Nelder–Mead optimization algorithm from VIP. This fitting process, involving the injection of synthetic sources with a negative flux at source location (Lagrange et al. 2010), aimed to minimize χ^2 residuals. (7) Once the parameters were determined, the position angle in the images was converted into the true position angle using the celestial north of NIRC2, which is $0°.262 \pm 0°.018$ (Service et al. 2016; see Franson et al. 2022 for an example and more details). (8) We converted the units of ρ from pixels to mas using the plate scale (see Section 3.1). (9) To derive the apparent magnitude of the sources (m_{cc}), we applied the following equation:

$$m_{\mathrm{cc}} = -2.5 \log_{10}(f_1/f_2) + m_{\mathrm{XRB}}, \qquad (1)$$

where f_2 is the PSF flux within the same aperture as the cube (3 FWHM) and m_{XRB} is the apparent magnitude of the X-ray

Table 1
Information on the Binary Nature for the 14 Observed X-Ray Binaries

Target (1)	Type (2)	Class (3)	Donor Star (4)	References (5)	Compact Object (6)	References (7)
RX J1744.7−2713	HMXB BeXRB γ Cas analog	N/A	B0.5III–Ve	(1)	WD[a]	(2)
IGR J18483−0311	HMXB SFXT XP	Outburst	B0.5-BI/B0-1Iab	(3, 4)	NS	(5)
γ Cas	HMXB BeXRB	Steady	B0.5IVe	(6, 7)	WD[a]	(8)
SAX J1818.6−1703	HMXB SFXT	Variable	B0.5Iab	(4)	NS[a]	(9)
1H 2202+501	HMXB BeXRB[a]	N/A	B3Ve	(10)	N/A	
4U 2206+543	HMXB	Variable	O9.5V	(11)	NS	(12)
4U 1700−377	sgHMXB	Variable	O6Iafpe	(13)	NS	(14)
IGR J17544−2619	HMXB SFXT	Flaring	O9Ib/O9IV–V	(15, 16, 17)	NS	(18)
RX J2030.5+4751	HMXB BeXRB γ Cas analog	N/A	B0.5III–Ve	(19)	N/A	
Cyg X-1	HMXB Microquasar	Variable	O9.7Iabpvar	(20)	BH	(21)
X Per	HMXB BeXRB XP	Variable	B0Ve	(22)	NS	(23)
1H 0556+286	HMXB[a]	N/A	B5ne	(24)	WD or NS	(25)
RX J0648.1−4419	HMXB XP	N/A	sdO5.5	(26)	WD	(27)
Vela X-1	HMXB XP	Variable	B0.5Ib	(28)	NS	(28)

Notes. Column (1): name of the target. Column (2): subclass/type of the X-ray binary, as found in Bird et al. (2016). Column (3): class of X-ray emission, as found in Krimm et al. (2013). Column (4): the spectral type of the donor star. Column (5): reference for the donor star. Column (6): the nature of the compact object. Column (7): reference for the compact object.
[a] Indicates an uncertain nature.

References. (1) Sarty et al. 2011; (2) Lopes de Oliveira et al. 2006; (3) Chaty et al. 2008; (4) Torrejón et al. 2010; (5) Sguera et al. 2007; (6) Moffat et al. 1973; (7) Raguzova & Popov 2005; (8) Postnov et al. 2017; (9) Walter & Zurita Heras 2007; (10) Simon et al. 2019; (11) Negueruela & Reig 2001; (12) Torrejón et al. 2004; (13) Sota et al. 2014; (14) Reynolds et al. 1999; (15) Pellizza et al. 2006; (16) Giménez-García et al. 2016; (17) Bikmaev et al. 2017; (18) in't Zand 2005; (19) Motch et al. 1997; (20) Sota et al. 2011; (21) Bolton 1972a; (22) Lyubimkov et al. 1997; (23) White et al. 1977; (24) Popper 1950; (25) Liu et al. 2006; (26) Jaschek & Jaschek 1963; (27) Popov et al. 2018; (28) Hiltner et al. 1972.

binary (see Section 3.3.2). (10) Using the known distance in parsecs (see Section 3.3.1), the apparent magnitude of the candidate CBCs (m_{cc}) was converted to absolute magnitude (M_{cc}) via the distance modulus equation. (11) Finally, to estimate the mass of the sources, we compared the absolute magnitude (M_{cc}) with evolutionary models from MESA Isochrones & Stellar Tracks (MIST; Paxton et al. 2011, 2013, 2015, 2018; Choi et al. 2016; Dotter 2016; Faherty et al. 2016) at the system's age (see Section 3.3.3).

Due to the poor quality of the PSF in our 2020 observations, we used the synthetic 2D PSF for fitting processes related to these observations. However, we kept the original PSF for our 2017 and 2018 observations. We conducted tests using both

synthetic and real PSFs on the 2017 and 2018 data, yielding consistent results. Consequently, the use of a synthetic PSF does not affect significantly the derived parameters.

The upcoming sections detail the acquisition of parameters used in the magnitude calculations.

3.3.1. Determining the Distance from the Observer

The distance from the observer is presented in the second column of Table 5 in the Appendix. Distances for 1H 2202 +501, 4U 2206+543, 4U 1700−377, IGR J17544−2619, Cyg X-1, X Per, and Vela X-1 were obtained from Zhao et al. (2023), which uses parallax measurements to infer distances using either an inversion or a Bayesian approach for a catalog

Table 2
Keck/NIRC2 Observing Log

UT Date	Target	Filter	WFS	t_{int} (s)	Coadds	N_{frames}	P.A. Cov. (deg)
2017 Sep 8	RX J1744.7−2713	L'	SH	0.5	60	40	14.3
	Cygnus X-1	L'	SH	0.5	60	140	60.6
	γ Cassiopeiae	L'	SH	0.18	150	130	61.2
	X Persei	L'	SH	0.5	60	89	43.9
2018 Jan 3	X Persei	L'	SH	1	45	54	36.7
	1H 0556+286	L'	SH	1	45	50	48.6
	RX J0648.1−4419	L'	SH	1	45	17	6.5
	Vela X-1	L'	SH	1	45	60	26.0
2020 Jul 11	RX J1744.7−2713	L'	py	0.5	60	120	38.3
	IGR J18483−0311	L'	py	0.4	60	125	42.6
	γ Cassiopeiae	L'	py	0.0528	400	150	48.1
2020 Jul 12	RX J1744.7−2713	K_s	py	0.6	45	92	39.6
	SAX J1818.6−1703	L'	py	0.4	60	90	26.3
	1H 2202+501	L'	py	0.4	60	89	36.9
	4U 2206+543	L'	py	0.4	60	27	49.5
2020 Jul 13	4U 1700−37	L'	SH	0.4	50	69	15.1
	IGR J17544−2619	L'	SH	0.4	50	94	36.5
	RX J2030.5+4751	L'	SH	0.4	60	132	53.9
	4U 2206+543	L'	SH	0.4	60	149	49.5

Note. Abbreviations are as follows: WFS—wave front sensor; SH—Shack–Hartmann; py—pyramid WFS; t_{int}—integration time; N_{frames}—number of frames; P.A. Cov.—parallactic angle coverage.

of X-ray binaries. For the other X-ray binaries, the distance was estimated through a photogeometric calculation (Bailer-Jones et al. 2021). It was calculated using the parallax measurement and its uncertainty (geometric), as well as the G magnitude and the $BP - RP$ color (photometric) from the Gaia Data Release 3 (DR3; De Angeli et al. 2023; Montegriffo et al. 2023). Table 3 presents the Gaia DR3 ID for each target. In cases where an object's distance was sourced from the literature, the respective reference is cited in the literature review of Section 2. As previously mentioned, this study targets X-ray binaries within ∼2–3 kpc accessible with Keck/NIRC2.

3.3.2. Determining the Apparent Magnitude of the Central X-Ray Binary

Observing X-ray binaries in the L' band of Keck/NIRC2 is not standard practice, making the direct determination of the true apparent magnitudes of the central X-ray binaries (m_{XRB}) unfeasible. Nonetheless, we leveraged the W1 filter from the Wide-field Infrared Survey Explorer (WISE), which has a central wavelength similar to Keck/NIRC2 L' band ($\lambda = 3.353\ \mu m$). Using the WISE Source Catalog (Wright et al. 2010), we approximated m_{XRB} for all X-ray binaries. These values are presented in the fifth column of Table 5 in the Appendix. To account for the differences between the two filters, we considered an uncertainty of 0.5 mag on m_{XRB}.

3.3.3. Determining the Age of the System

Most X-ray binaries in our sample lack age estimates in the literature, except for RX J1744.7−2713 (up to ∼60 Myr; Coleiro & Chaty 2013), 4U 1700−377 (up to ∼80 Myr; Coleiro & Chaty 2013), γ Cas (8.0 ± 0.4 Myr; Zorec et al. 2005), Cyg X-1 (<4 Myr; Miller-Jones et al. 2021), and X Per (∼5 Myr; Lyubimkov et al. 1997). For the remaining X-ray

Table 3
Gaia DR3 ID for Each Target

Target	Gaia DR3 ID
RX J1744.7−2713	4060784345959549184
IGR J18483−0311	4258428501693172736
γ Cas	426558460884582016
SAX J1818.6−1703	4097365235226829312
1H 2202+501	1979911002134040960
4U 2206+543	2005653524280214400
4U 1700−377	5976382915813535232
IGR J17544−2619	4063908810076415872
RX J2030.5+4751	2083644392294059520
Cyg X-1	2059383668236814720
X Per	168450545792009600
1H 0556+286	3431561565357225088
RX J0648.1−4419	5562023884304070000
Vela X-1	5620657678322625920

binaries, we established an upper limit using basic evolutionary models and the spectral type of the donor star (see Table 1). We found the maximum age that the donor star can reach before exploding in supernovae. However, this approach provides only an approximate estimation of the age. These values are presented in the sixth column of Table 5 in the Appendix.

3.3.4. Determining the Errors

Errors in the fit parameters (θ, ρ, and f_1) were estimated using an injection/recovery approach (see Prasow-Émond et al. 2022). This approach relies on injecting synthetic sources with known parameters into the images. Subsequently, the same optimization method was applied (see Section 3.3), and the error was determined as the difference between estimated and known parameters. This method was employed across a range

of parameter values to ensure consistency; it was observed that errors were more pronounced for smaller offset values (i.e., those closer to the central X-ray binary). Additional sources of uncertainty were taken into consideration in cases where the value of a parameter is expected to remain consistent between two sets of observations, specifically astrometric parameters in two different bands. The dominant source of uncertainty was defined as the total uncertainty.

4. Key Properties of the Sample

4.1. γ Cassiopeiae

γ Cassiopeiae—also known as 2S 0053+604 (hereafter γ Cas)—harbors a well-studied optical component classified as a Be star (Moffat et al. 1973). Its X-ray luminosity ($\sim10^{32}$–10^{33} erg s^{-1}; Raguzova & Popov 2005) is higher than the typical luminosity for O/B stars ($\sim10^{30}$ erg s^{-1}) but too low to be a Be/NS system ($\sim10^{34}$ erg s^{-1} in quiescence; Shrader et al. 2015). The nature of the system can be explained by two hypotheses: (1) the system is an HMXB, involving accretion onto a WD or a fast-spinning NS (Postnov et al. 2017); or (2) the excess of X-ray emission stems from physical processes in the high atmosphere of γ Cas (Kubo et al. 1998; Robinson & Smith 2000). Though γ Cas is not confirmed as being an HMXB, its resemblance to other sources, referred to as γ Cas analogs, warranted its inclusion in our sample. Located at a distance of 0.19 ± 0.02 kpc, it is the nearest system in our sample. Its proximity and proper motions (25.7 ± 0.5 mas yr^{-1} in R.A., -3.9 ± 0.4 mas yr^{-1} in decl.; Perryman et al. 1997) allowed us to conduct a proper-motion analysis within the interval between our two observation sets (see Section 6.2).

4.2. RX J1744.7−2713

RX J1744.7-2713 is classified as a BeXRB (Israel et al. 1997) and is composed of a B0.5III–Ve star (Motch et al. 1997; Steele et al. 1999; Lopes de Oliveira et al. 2006) and a WD. However, the origin of X-ray emission is still uncertain and debated in the literature (Lopes de Oliveira et al. 2006). It is also known as a γ Cas analog, due to the similarities in their X-ray properties (e.g., Shrader et al. 2015). The first high-contrast images of this HMXB were presented in Prasow-Émond et al. (2022), in which more comprehensive information on the system can be found.

4.3. 4U 1700−377

4U 1700−377, discovered with the Uhuru X-ray satellite, is classified as an HMXB (Jones et al. 1973). The system contains a supergiant donor star of spectral type O6Iafpe (Sota et al. 2014) and a magnetized NS (e.g., Reynolds et al. 1999; Bala et al. 2020; van der Meij et al. 2021) exhibiting strong flaring activity (e.g., Kuulkers et al. 2007). This HMXB was observed with, e.g., XMM-Newton (van der Meer et al. 2005; Giménez-García et al. 2015), Chandra (Boroson et al. 2003; Martínez-Chicharro et al. 2021), the Hubble Space Telescope (Hainich et al. 2020), the Fiber-fed Extended Range Optical Spectrograph (Hainich et al. 2020), IUE (Dupree et al. 1978), EXOSAT (Haberl et al. 1989), BATSE (Rubin et al. 1996), and BeppoSAX (Reynolds et al. 1999). NGC 6231, located within the OB association Sco OB1, has been recently confirmed as the parent cluster of 4U 1700−377 (van der Meij et al. 2021). Moreover, Coleiro & Chaty (2013) inferred an estimated age of

~80 Myr for the system, a value we have regarded as an upper limit as in Prasow-Émond et al. (2022). Its X-ray luminosity can reach up to $\sim7 \times 10^{36}$ erg s^{-1} (Laurent et al. 1992).

4.4. 4U 2206+543

Although the nature of its donor star remains uncertain (first believed to be of spectral type Be, Steiner et al. 1984; then O9.5V, Negueruela & Reig 2001), 4U 2206+543 is a well-studied HMXB harboring a magnetar NS (e.g., Torrejón et al. 2004, 2018; Blay et al. 2005; Reig et al. 2009; Ikhsanov & Beskrovnaya 2010). First discovered with Uhuru (Giacconi et al. 1972), the system was subsequently observed with, e.g., EXOSAT (Saraswat & Apparao 1992), RXTE (e.g., Corbet & Peele 2001), IBIS/ISGRI on INTEGRAL (e.g., Bird et al. 2004), BeppoSAX (e.g., Masetti et al. 2004), the Very Large Array (Blay et al. 2005), Swift (Corbet et al. 2007), and Suzaku (Finger et al. 2010). Its X-ray luminosity ranges from $\sim10^{33}$ erg s^{-1} in quiescence up to $\sim10^{35}$–10^{36} erg s^{-1} during more active phases (Ribó et al. 2006).

4.5. RX J2030.5+4751

RX J2030.5+4751, also known as BD +47°3129 and SAO 49725, was first discovered with ROSAT (Motch et al. 1997). It is identified as a BeXRB and γ Cas analog. It has a B0.5III–Ve spectral type donor star and a maximum X-ray luminosity of $\sim10^{33}$ erg s^{-1} (Liu et al. 2006; Raguzova 2007). XMM-Newton/EPIC observations have revealed that RX J2030.5 +4751 has a hard X-ray spectrum, suggesting the presence of a dense, large, and stable circumstellar environment surrounding the system (Lopes de Oliveira et al. 2006). On 2016 July 20, RX J2030.5+4751 underwent type I (i.e., smaller and repetitive) bursts, reaching its maximum luminosity (progressive weakening since; Steele 2016a, 2016b, 2016c). Regarding the long-term variability, Servillat et al. (2012) reported a significant nonperiodic variability of approximately 1 mag in the light curve of RX J2030.5+4751 over ~100 yr, likely caused by changes in the properties of the decretion disk.

4.6. 1H 2202+501

1H 2202+501 is a poorly studied HMXB, albeit appearing in some surveys (e.g., Wood et al. 1984; Hanson et al. 1996; Liu et al. 2000). It consists of a Be star of spectral type B3Ve (Simon et al. 2019), and the nature of the compact object remains uncertain. Its X-ray luminosity is estimated to be $\sim9 \times 10^{32}$ erg s^{-1} (Chevalier & Ilovaisky 1998).

4.7. SAX J1818.6−1703

SAX J1818.6−1703 was discovered with BeppoSAX while undergoing a strong outburst (in't Zand et al. 1998). Subsequent observations were carried out using IBIS/ISGRI on board INTEGRAL (e.g., Grebenev & Sunyaev 2005; Sguera et al. 2005; Zurita Heras & Chaty 2009; Sidoli et al. 2016), RossiXTE (Sguera et al. 2005; Smith et al. 2012), and Swift (e.g., Bird et al. 2009; Sidoli et al. 2009). The system has similar properties to other SFXTs (e.g., Sguera et al. 2005; Negueruela & Smith 2006; Sidoli et al. 2009; Bozzo et al. 2012), and its compact object is likely an NS (e.g., Walter & Zurita Heras 2007; Boon et al. 2016). The donor star of the system, confirmed by Chandra (in't Zand et al. 2006), is classified as a supergiant star of spectral type B0.5Iab (Torrejón

et al. 2010). Also observed using XMM-Newton, SAX J1818.6 −1703 has a quiescent X-ray luminosity that can drop to values below ∼10^{32} erg s^{-1} (as determined by not being detected in Bozzo et al. 2012) and can reach up to ∼8×10^{35} erg s^{-1} (Torrejón et al. 2010).

4.8. IGR J18483−0311

Discovered with IBIS/ISGRI on board INTEGRAL by Chernyakova et al. (2003), IGR J18483−0311 is a well-studied SFXT (Rahoui & Chaty 2008) composed of an X-ray pulsar (Sguera et al. 2007) and a supergiant donor star of spectral type B0.5Ia (Chaty et al. 2008) or B0.5–B1Iab (Torrejón et al. 2010). The system undergoes multiple short and long outbursts (e.g., Sguera et al. 2007, 2010; Ducci et al. 2013; Sguera et al. 2015), resulting in its X-ray luminosity ranging from ∼10^{33}– 10^{34} erg s^{-1} in quiescence (Romano et al. 2010; Sguera et al. 2015) up to ∼10^{36} erg s^{-1} during its strongest flares (Torrejón et al. 2010). By considering evolutionary scenarios and exploring the relationship between spin and orbital periods, Liu et al. (2011) suggested that the compact object in IGR J18483−0311 may originate from an O-type emission-line star rather than an average main-sequence star.

4.9. IGR J17544−2619

IGR J17544−2619 was first discovered near the Galactic center while undergoing short (a few hours) outbursts using IBIS/ISGRI on board INTEGRAL (Grebenev et al. 2003, 2004; Sunyaev et al. 2003). The system was subsequently observed with, e.g., XMM-Newton (Drave et al. 2014; González-Riestra et al. 2004), Chandra (in't Zand 2005), EMMI/SOFI/NTT (Pellizza et al. 2006), Suzaku (Rampy et al. 2009), RXTE (Drave et al. 2012), Swift (e.g., Romano et al. 2015), and NuSTAR (e.g., Bhalerao et al. 2015). It is identified as an SFXT (Negueruela et al. 2006), and the optical/near-infrared counterpart is a massive star of spectral type O9Ib (25–28 $M_\odot$; Pellizza et al. 2006; Giménez-García et al. 2016) or O9IV–V (23 $M_\odot$; Bikmaev et al. 2017). The compact object is an NS (in't Zand 2005), as inferred by the presence of a cyclotron line at 17 keV and the magnetic field strength (∼1.5×10^{12} G, typical for NSs in X-ray binaries; Bhalerao et al. 2015). The change in X-ray luminosity between quiescence and outburst is significant, ranging from $L_X \sim 10^{32}$–10^{34} erg s^{-1} (e.g., Bozzo et al. 2016) during quiescence to a maximum of $L_X \sim 3 \times 10^{38}$ erg s^{-1} during outburst (Romano et al. 2015).

4.10. Cyg X-1

Cygnus X-1 (hereafter Cyg X-1), first discovered in 1964, is one of the most well-studied astronomical objects (e.g., Fabian et al. 1989; Esin et al. 1998; Orosz et al. 2011; Tomsick et al. 2014; Parker et al. 2015; Sell et al. 2015; Walton et al. 2016; Mastroserio et al. 2019). The system's compact object, with a mass of 21.2 ± 2.2 $M_\odot$ (Miller-Jones et al. 2021), was the first observed candidate BH (Murdin & Webster 1971; Bolton 1972a), leading to significant breakthroughs in the astronomical scientific community. Cyg X-1 is classified as an HMXB (Bolton 1972b), and the donor star is characterized as a massive star of spectral type O9.7Iabpvar (Sota et al. 2011). The system is fairly young, with an estimated age of 5 ± 1.5 Myr in Mirabel & Rodrigues (2003) and <4 Myr in Miller-Jones et al. (2021). Cyg X-1 is located at $2.22^{+0.17}_{-0.18}$ kpc; its distance from

the observer was precisely estimated in Miller-Jones et al. (2021) based on radio parallax measurements and validated with Gaia DR3. The microquasar undergoes variable X-ray emission (Krimm et al. 2013), with a maximum X-ray luminosity of ∼3×10^{37} erg s^{-1} (Di Salvo et al. 2001).

4.11. Vela X-1

Vela X-1 is a pulsing HMXB discovered with the Uhuru X-ray satellite (Giacconi et al. 1971) and was observed through multiple surveys and with several instruments (e.g., Charles et al. 1978; La Barbera et al. 2003; Fürst et al. 2014; Martínez-Núñez et al. 2014). The system is highly variable and undergoes transient outbursts and X-ray eclipses (e.g., van der Klis & Bonnet-Bidaud 1984). Its X-ray luminosity can be as high as 4×10^{36} erg s^{-1} (Kreykenbohm et al. 2008). It is composed of a B0.51b donor star (Hiltner et al. 1972) and of a magnetized NS (e.g., Hiltner et al. 1972; van Kerkwijk et al. 1995; Kreykenbohm et al. 2002; Diez et al. 2022). A complete review of this object can be found in Kretschmar et al. (2021).

4.12. RX J0648.1−4419

RX J0648.1−4419 is a unique X-ray pulsating system, as it is the only HMXB known to date containing a hot subdwarf donor star of spectral type O (sdO5.5; Jaschek & Jaschek 1963; Mereghetti et al. 2009). The compact object has a mass of 1.28 ± 0.05 $M_\odot$ (Mereghetti et al. 2009) and was initially believed to be an NS (e.g., Israel et al. 1997; Mereghetti et al. 2016). Popov et al. (2018) suggested that it was likely a young (∼2 Myr) contracting WD. Over the course of almost 30 yr of observations (e.g., Mereghetti et al. 2011, 2021; La Palombara et al. 2015), the X-ray luminosity remained stable, maintaining a value of ∼10^{32} erg s^{-1}.

4.13. 1H 0556+286

1H 0556+286 contains a Be star of spectral type B5ne (Popper 1950). It is a poorly studied system; while it is generally thought to be an HMXB (e.g., Helfand & Moran 2001; Liu et al. 2006), Torrejón & Orr (2001) presented BeppoSAX observations in which no X-ray emission was detected. As per these results, neither the Be/NS nor Be/WD scenarios appear probable; hence, the nature of the system remains unclear.

4.14. X Per

X Persei (hereafter X Per), also known as 4U 0352+309, was discovered in 1972 with the Copernicus Observatory (Hawkins et al. 1975; Mason et al. 1976). The system was subsequently observed with, e.g., the High Energy Astrophysical Observatory (HEAO 2/Einstein; Weisskopf et al. 1984), RXTE (e.g., Delgado-Martí et al. 2001; Coburn et al. 2002), INTEGRAL (e.g., Lutovinov et al. 2012), XMM-Newton (e.g., La Palombara & Mereghetti 2007), and Chandra (e.g., Valencic & Smith 2013). The system is identified as an HMXB/BeRB, composed of a magnetized NS as the compact object (e.g., White et al. 1977; Coburn et al. 2001; Doroshenko et al. 2012; Maitra et al. 2017; Yatabe et al. 2018) and a Be star of spectral type B0Ve as the donor star (Lyubimkov et al. 1997). In quiescence, its X-ray luminosity is ∼10^{34} erg s^{-1} (e.g., Coburn et al. 2001). When undergoing strong outburst activity, its X-ray luminosity can reach up to

$\sim 2 \times 10^{35}$ erg s^{-1} (Lutovinov et al. 2012). Similarly to Cyg X-1, the system is also relatively young, with an estimated age of ~ 5 Myr (Lyubimkov et al. 1997). Objects with similar properties are often referred to as X Per analogs.

5. High-contrast Images

5.1. γ Cas

As discussed in Section 4.1, observations of γ Cas in the L' band were initially made on 2017 September 8 and subsequently revisited almost 3 yr later on 2020 July 11. Figure 2 presents the L'-band high-contrast images of γ Cas for both epochs. A bright source, labeled B, was detected with an S/N $\gg 5$. A much fainter source, labeled C, was also detected, with an S/N ~ 3. In Section 6.2, we undertake a proper-motion analysis to determine whether these sources are more likely to be bound CBCs or background stars.

5.2. Other X-Ray Binaries

Figure 3 presents a panel of L'-band high-contrast images of all the other X-ray binaries, in order: 4U 1700$-$377, 4U 2206 $+$543, RX J2030.5$+$4751, 1H 2202$+$501, SAX J1818.6 $-$1703, IGR J18483$-$0311, IGR J17544$-$2619, Cyg X-1, Vela X-1, RX J0648.1$-$4419, 1H 0556$+$286, and X Per. The L'- and K_s-band images of RX J1744.7$-$2713 can be found in Prasow-Émond et al. (2022). By inspecting the images, we determined that 4U 2206$+$543, Vela X-1, RX J0648.1$-$4419, and 1H 0556$+$286 do not exhibit any potential candidate CBCs. Consequently, further analysis of these systems will not be pursued, except for the calculation of companion frequency in Section 6.3. Among the remaining X-ray binaries, we successfully detected at least one source for each system with a significantly large S/N (>5). These sources are labeled in the images, starting from the letter B.

Table 6 in the Appendix presents several physical properties of the detected sources, including the angular separation in mas, the position angle in degrees, the apparent magnitude in L' band, and the mass estimated from evolutionary models.

In the next sections, we analyze the nature of the detected sources and discuss the implications of the results.

6. On the Nature of the Detected Sources

6.1. Background Contamination

We used TRILEGAL (Girardi et al. 2005) to discriminate background/foreground stars from gravitationally bound CBCs. TRILEGAL is a 3D model employed to simulate the photometric properties of star fields within the Galaxy (e.g., Chun et al. 2015; Dietrich & Ginski 2018; Jones et al. 2021; Williams et al. 2021). We compiled a list of predicted sources within a 1×1 arcmin^2 region surrounding the X-ray binary using its R.A./decl. coordinates. Subsequently, we applied a geometric rescaling so that the TRILEGAL FOV matches the FOV of the high-contrast images (10.24×10.24 arcsec^2) for statistical consistency. We calculated the cumulative distribution of the expected number of sources in the FOV below an apparent magnitude ($m_{L'}$), for the distribution of apparent magnitudes ($\mathcal{L}'$). It is denoted as $n_{\mathrm{FOV}}(\mathcal{L}' \leqslant m_{L'})$.

Figure 4 presents $n_{\mathrm{FOV}}(\mathcal{L}' \leqslant m_{L'})$ as a function of $m_{L'}$ for both TRILEGAL and the detected sources in the high-contrast images. It includes all X-ray binaries with detected sources, except γ Cas (for which the confirmation of the nature of the

CBCs relies primarily on proper-motion analysis) and RX J1744.7$-$2713 (presented in Prasow-Émond et al. 2022). In Appendix Table 6, we listed $n_{\mathrm{FOV}}(\mathcal{L}' \leqslant m_{L' \text{ source}})$ for each detected source. This represents the expected number of sources—based on TRILEGAL simulations—with apparent magnitudes ($m_{L'}$) below the magnitude of the corresponding source ($m_{L' \text{ source}}$) while accounting for errors. If the calculated value, including the upper limit, was lower than the total number of sources detected below $m_{L' \text{ source}}$, we reject the hypothesis of background/foreground contamination for that particular source.

Many sources were not predicted by TRILEGAL. Specifically, all detected sources in 4U 1700$-$377, RX J2030.5 $+$4751, Cygnus X-1, X Per, and 1H 2202$+$501 were not expected from the model given their magnitudes and would thus suggest that they are bound to the X-ray binary. The FOVs of IGR J17544$-$2619 and SAX J1818.6$-$1703 were expected to be more populated than what we detected, suggesting that the detected sources are likely background or foreground contaminants. The disparity between the predicted and observed number of sources might result from the elimination of stationary sources during the ADI process or from an insufficient S/N for detection. In the case of IGR J18483 $-$0311, sources B, C, and F might be CBC candidates, but their status remains uncertain in the current stage of our study.

We extended our analysis by calculating the probability of chance alignment for each detected source. This probability represents the likelihood that these sources are not associated with the X-ray binary system based on the angular separation and the density on the sky of unrelated objects. This method assumes that the distribution of unrelated sources across the area follows a Poisson distribution. Note that this method usually relies on sky surveys such as the Two Micron All Sky Survey Point Source Catalog (e.g., Correia et al. 2006; Lafrenière et al. 2008, 2014; Prasow-Émond et al. 2022) to establish the distribution of unrelated objects. However, in this work we used TRILEGAL as an alternative owing to the absence of available K_s-band observations.

To calculate the aforementioned probability, we first divided the cumulative distribution of the number of sources $n_{\mathrm{TRILEGAL}}(\mathcal{L}' \leqslant m_{L'})$ by the area from which the sources were retrieved (between 6×6 arcmin^2 and 15×15 arcmin^2 depending on the location of the X-ray binary). This division enabled us to derive a surface density denoted as Σ. Using the angular separation Θ in arcsec, the probability of a source being drawn from the TRILEGAL distribution—thus indicating its lack of association with the central X-ray binary—is given by

$$P_{\mathrm{unrelated}}(\Sigma, \Theta) = 1 - \exp(-\pi \Sigma \Theta^2). \qquad (2)$$

In Appendix Table 6, we listed $1 - P_{\mathrm{unrelated}}(\Sigma, \Theta)$ as percentages. Many sources have high probabilities ($>85\%$) of being associated with the central X-ray binary. However, some sources have lower probabilities (between 65% and 75%) that are not as statistically significant, but we nevertheless identified them as candidate CBCs given the early stage of the study. Sources with probabilities below 60% (not statistically significant) were rejected as candidate CBCs.

6.2. Proper-motion Analysis: γ Cas

Conducting a proper-motion analysis is among the most robust methods for confirming the gravitational association
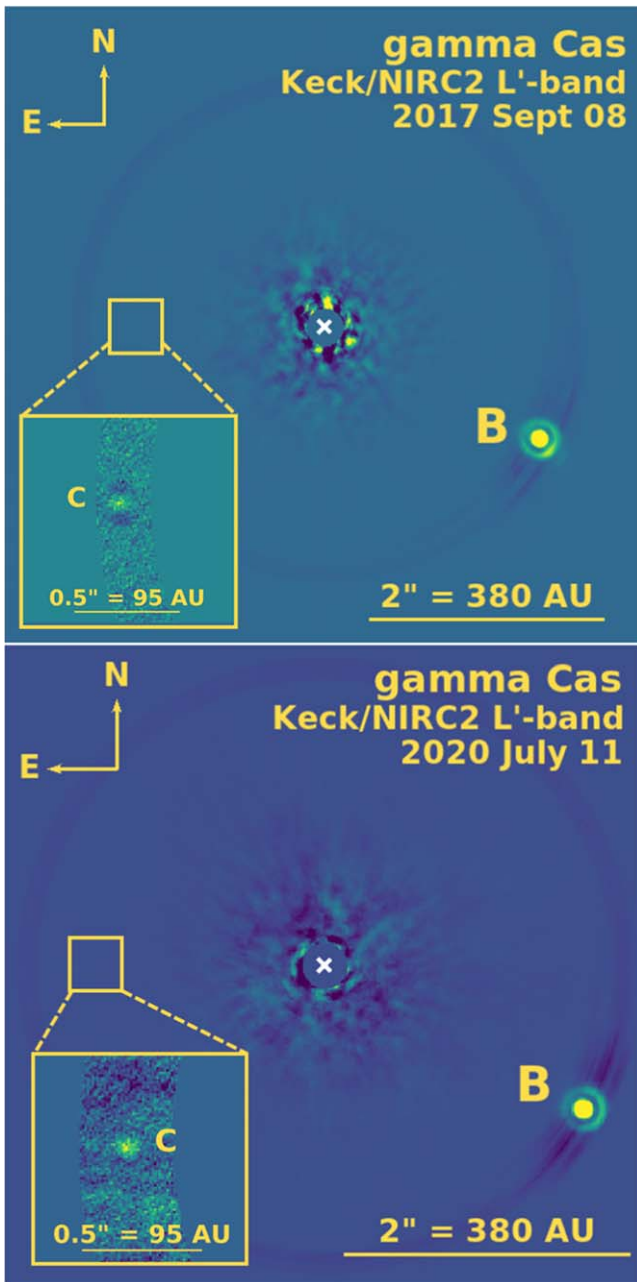
Figure 2. Keck/NIRC2 L'-band high-contrast images of γ Cas acquired on 2017 September 8 (up) and 2020 July 11 (bottom), treated and reduced using a PCA annular ADI algorithm (using `VIP`; Gomez Gonzalez et al. 2017). The sources detected with S/N > 3 are labeled B and C. The white cross denotes the approximate position of γ Cas, masked by the coronagraph. The insets in the lower left corners show zoomed-in high-contrast images with a focus on an annular region (obtained using the PCA annulus algorithm in `VIP`), highlighting the presence of the fainter source (labeled as C).

of a source with the system (e.g., Bohn et al. 2021). Given the proximity of γ Cas and its proper motions (see Section 4.1), it was possible to conduct a statistically significant proper-motion analysis between the two observed epochs (2017 September 8 and 2020 July 11). Figure 5 presents the relative separations between sources B, C, and γ Cas in R.A. and decl., alongside the expected position of a stationary background star. The figure also displays the angular separation and position angle over time, along with the expected tracks for both comoving and stationary background objects.

Source B's trajectory implies an underlying motion that necessitates additional epochs of observation for validation. In 2020, the angular separation data point aligns with the comoving track, but the position angle data point deviates by $\sim 3\sigma$ from the same track. This trajectory suggests that source B is more likely to be bound to γ Cas rather than an unrelated background or foreground object. Nonetheless, its motion suggests potential scenarios such as orbital motion, ejection from the system, or the presence of a nonstationary background or foreground object. Using the mass of γ Cas ($\sim 13\,M_\odot$; Nemravová et al. 2012) and the radial separation of source B, we calculated the escape velocity as $v_{\rm esc} = \sqrt{2GM/\rho} \approx 7680\,{\rm m\,s^{-1}}$. Additionally, the projected velocity between 2017 and 2020 was determined, resulting in the vector $v_{\rm proj} \approx (1670\,\hat{\rho} - 17964\,\hat{\theta})\,{\rm m\,s^{-1}}$. Since the norm of the velocity vector is greater than the escape velocity, source B appears to be physically associated with γ Cas, but it is not bound (as also suggested in Hutter et al. 2021). A comprehensive characterization of this motion using high-contrast imaging necessitates further epochs of observation.

Source C consistently follows the motion track of an unrelated object across all three plots. Thus, we excluded it from our list of candidate CBCs with a $\gg 3\sigma$ confidence level.

6.3. Frequency of Multiple Systems and Companion Frequency

Two key concepts are commonly defined in the stellar multiplicity literature (e.g., Duchêne & Kraus 2013): the frequency of multiple systems (MF) and the companion frequency (CF; i.e., the average number of companions per target). While a proper-motion analysis is required to confirm most of the sources, we calculated a first estimation of MF and CF for the observed X-ray binaries in our sample. Among the total of 14 observed X-ray binaries, we have identified candidate CBCs in eight systems: 4U 1700−377, RX J2030.5+4751, Cyg X-1, X Per, 1H 2202+501, γ Cas, RX J1744.7−2713, and IGR J18483−0311. Thus, based on these numbers and at this stage of the study, MF for triple or higher-tier systems would be $8/14 \approx 0.6$ ($\sim 60\%$). For CF, it is important to note that X-ray binaries inherently possess one companion, the donor star, which is included in our calculation of CF. Based on the status of the detected sources listed in Appendix Table 6, the calculated average number of companions per compact object is 2.1 ± 1.1 ($210\% \pm 110\%$). This means that, on average, the compact object has two companions (the donor star and one additional companion). However, this value reduces to 1.8 ± 0.9 ($180\% \pm 90\%$) when considering only the sources that are most likely to be gravitationally bound $(1 - P_{\rm unrelated}(\Sigma,\ \Theta) > 85\%)$. These values are subject to change as new observations become available and further analyses are conducted.

7. Discussion

7.1. Stellar Multiplicity

The discovery of candidate CBCs would imply that X-ray binaries can still be produced by multiple-star systems rather than exclusively binary systems. The total mass (i.e., compact object and donor star) of all the HMXBs in our sample exceeds $\sim 10\,M_\odot$, with some reaching up to around $60\,M_\odot$, placing them on the higher end of the mass spectrum. Stellar multiplicity is believed to be common in high-mass star systems (e.g., Chini et al. 2012; Duchêne & Kraus 2013), and high-order multiplicity is thought to increase with primary
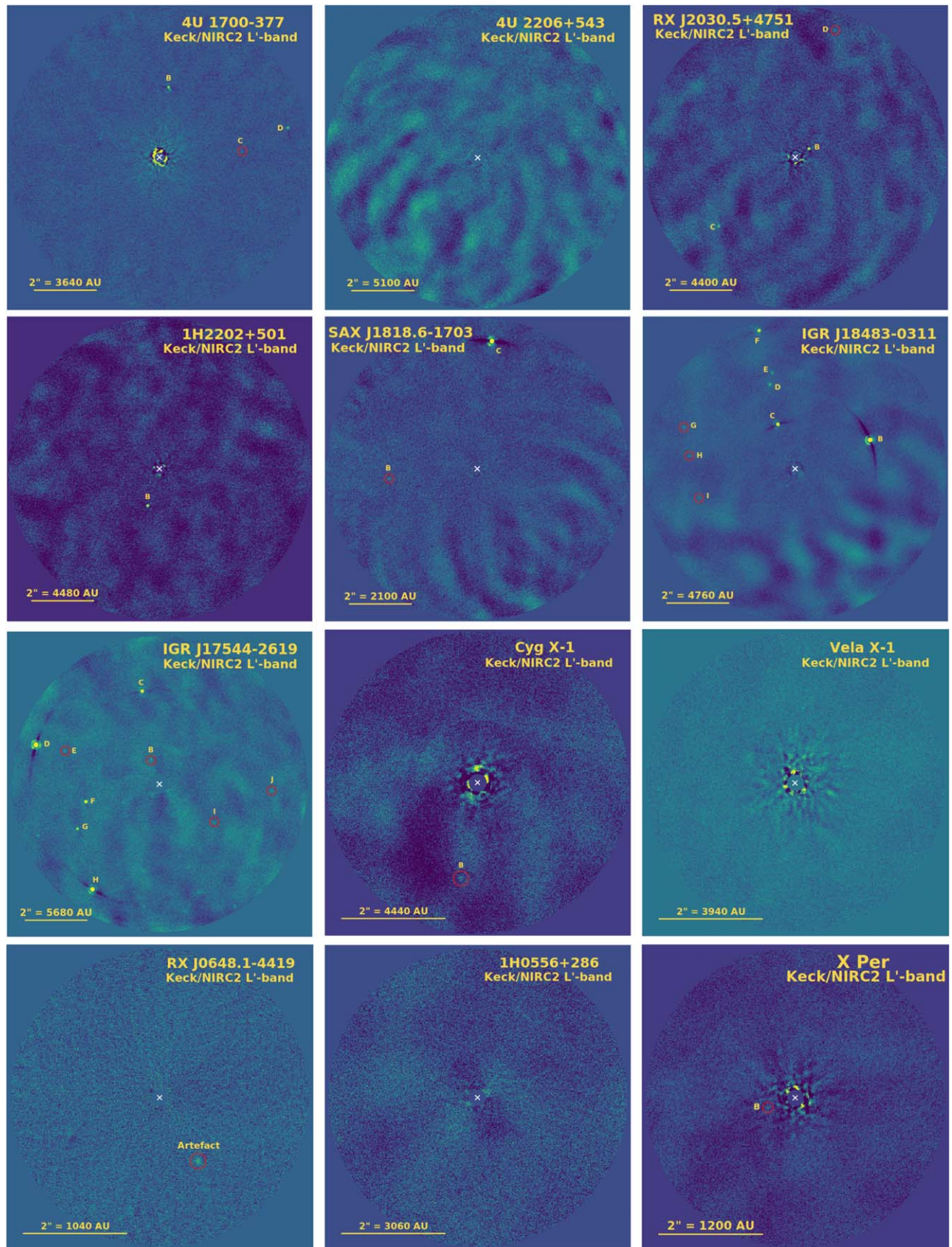
Figure 3. Keck/NIRC2 L'-band high-contrast images of all observed X-ray binaries—except RX J1744.7−2713 (see Prasow-Émond et al. 2022) and γ Cas (see Figure 2)—acquired on 2017 September 8, 2018 January 3, and 2020 July 11–13. Images were treated and reduced using a PCA annular ADI algorithm (using VIP; Gomez Gonzalez et al. 2017). The sources detected with S/N > 5 when computing the S/N map are labeled. The white cross denotes the position of the X-ray binary masked by the coronagraph. North points upward, and east points to the left, as in Figure 2.
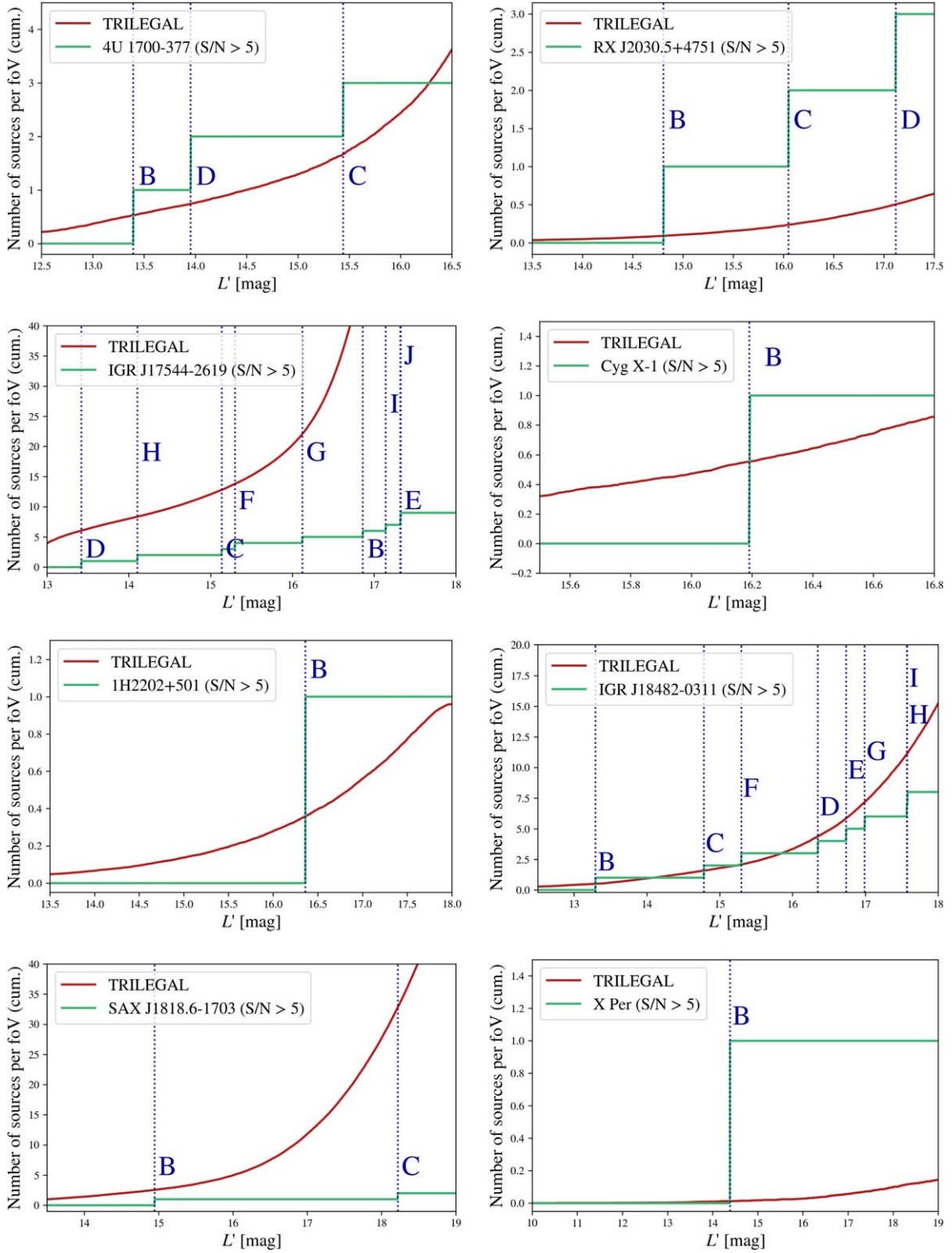
Figure 4. Cumulative distribution of the number of sources in the FOV expected from TRILEGAL simulations (red) and detected with an S/N > 5 in the high-contrast images (green) as a function of the apparent magnitude $m_{L'}$. It includes all X-ray binaries in which sources were detected except γ Cas and RX J1744.7−2713 (see Prasow-Émond et al. 2022): 4U 1700−377, RX J2030.5+4751, IGR J17544-2619, Cygnus X-1, 1H 2202+501, IGR J18483−0311, X Per, and SAX J1818.6−1703.

mass (e.g., Peter et al. 2012). However, surveys for high-mass stars remain incomplete.

For high-mass stars ($\gtrsim 16\,M_\odot$), MF and CF are estimated to be $\geqslant 80\%$ and $130\% \pm 20\%$, respectively (Chini et al. 2012; Duchêne & Kraus 2013). The first estimation of MF for our

sample ($\sim 60\%$; calculated in Section 6.3) falls below this percentage. However, in this study, MF is constrained by the range of projected separations (up to $\sim 12,000$ au). This implies that increasing this limit could potentially lead to the discovery of more companions and hence increasing the estimation of
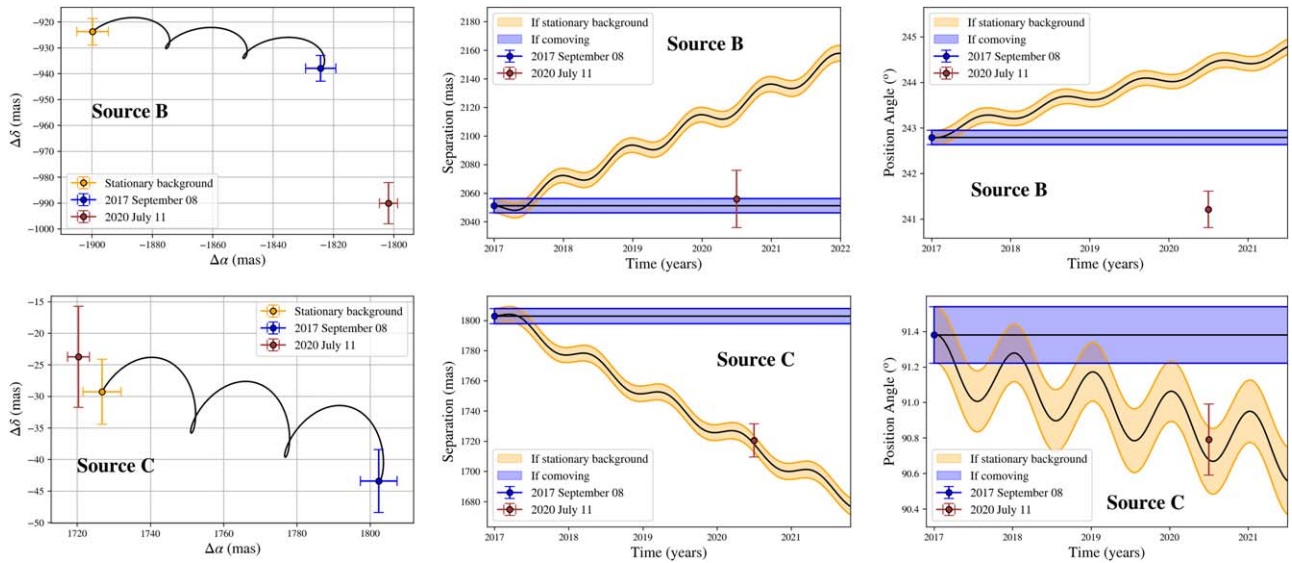
Figure 5. Left: relative separations between source B (top row), source C (bottom row), and γ Cas in R.A. (α) and decl. (δ). The first-epoch astrometric point is plotted in blue (2017 September 8), and the second-epoch astrometric point is plotted in red (2020 July 11). The expected position for a stationary background object is plotted in yellow, along with its proper-motion track. Middle: separation from γ Cas in mas as a function of time. A background object with zero proper motion would follow the orange track, while a bounded and comoving CBC would lie within the blue zone. Right: same as the middle panels, but for the position angle in degrees.

MF. As for CF ($210\% \pm 110\%$; calculated in Section 6.3), it currently exceeds the estimate obtained from the literature ($130\% \pm 20\%$; Chini et al. 2012). Further observations will likely lead to the rejection of candidate CBCs we have detected, which would lower the sample's CF (along with the associated uncertainty range). In both cases, our preliminary estimations (MF and CF) seem to be broadly in line with current estimates in the literature.

For solar-type stars, the frequency $N(n)$ of multiplicity n follows a geometric distribution $N(n) \sim \beta^{-n}$ (up to $n = 7$ with $\beta = 2.3$ or 3.4; Eggleton & Tokovinin 2008). Such a relation has not been derived for massive stars. Thus, the results from this study could be used to derive one, allowing us to predict the frequency of multiplicity in X-ray binaries and high-mass systems. The current sample size may be insufficient to infer a statistically significant relationship, but these results can still contribute valuable data to future surveys of high-mass systems.

This pilot study, in addition to showing evidence for potential additional components in X-ray binaries, could contribute to stellar multiplicity surveys for massive stars. It could also enable us to probe stellar multiplicity at low mass ratios (below ~ 0.1).

7.2. Stability in Wide Orbit

The projected separations within the scope of this study (from ~ 350 to $\sim 12,000$ au) would suggest that CBCs orbit at very large distances from the central X-ray binary. Note that CBCs located closer to the X-ray binary within the 2–3 kpc distance range cannot currently be detected through direct imaging. To assess whether potential CBCs could be gravitationally bound to these systems, we calculated the binding energy $E_{\rm bind}$ for every source likely to be a CBC. Assuming circular orbits, $E_{\rm bind}$ is estimated using the following equation (e.g., Naud et al. 2014; Prasow-Émond et al. 2022):

$$E_{\rm bind} \sim -\frac{GM_{\rm XRB}M_{\rm comp}}{1.27r}, \qquad (3)$$

where G is the gravitational constant, $M_{\rm XRB}$ is the total mass of the central X-ray binary, $M_{\rm comp}$ is the mass of the CBC, r is the

projected separation between the CBC and the X-ray binary, and 1.27 is the average projection factor between r and the semimajor axis assuming a random viewing angle (e.g., Brandeker et al. 2006).

The binding energies for each candidate CBC range from roughly -2×10^{42} erg to -3×10^{44} erg. A binding energy of roughly -10^{41} erg was obtained for the comoving exoplanet GU Psc b around an M3 spectral type star ($\sim 0.46\,M_\odot$), with a mass of $\sim 9M_{\rm Jup}$–$13M_{\rm Jup}$ and located at a distance of ~ 2000 au (Naud et al. 2014). All candidate CBCs have binding energies largely exceeding this currently known lower limit. This suggests that these sources, if confirmed as CBCs, would fall within the gravitational binding range of the X-ray binary.

We must also consider dynamic stability for systems containing more than one candidate CBC. N-body simulations have shown that a configuration of two CBCs at the same projected separation from the central system can lead to dynamic instability (e.g., Kiseleva et al. 1994). Thus, in the case of 4U 1700$-$377, where B and C have similar projected separations, configurations B+D and C+D are more likely than B+C+D. As for RX J2030.5+4751 and IGR J18483$-$0311, the candidate CBCs have distant projected separations, suggesting that configurations B+C and B+C+D, respectively, are plausible.

7.3. Companion Formation and Capture Scenarios

If our findings are confirmed, we hypothesize that CBCs orbiting X-ray binaries could originate through two main mechanisms: (1) formation within the same environment as the central X-ray binary, or (2) capture by the system. On the one hand, as detailed in Prasow-Émond et al. (2022), there are three scenarios in which CBCs could potentially form in the direct environment of X-ray binaries, and these scenarios may unfold at different times. First, CBCs could have formed simultaneously with the initial stars that subsequently evolved to form the present X-ray binary, resulting from the direct fragmentation of a collapsing prestellar core (e.g., Bate 2012). Note that this scenario is unlikely because we would expect companions with a mass similar to that of the main X-ray binary. Second,

Table 4
Recommended Year for Follow-up Observations for Every X-Ray Binary with at Least One Candidate CBC—Calculated Using the Distance, Proper Motions, and Astrometric Errors on the 2020 Observations—Enabling a Proper-motion Analysis at a $>3\sigma$ Significance Level

Target	Recommended Year
X Per	2026
Cyg X-1	2024
IGR J18483−0311	2024
1H 2202+501	2027
4U 1700−377	2024
RX J2030.5+4751	2024

their formation might have occurred within the circumbinary disk surrounding the initial binary system, prior to the supernova explosion of the now-compact object (e.g., Kratter et al. 2010). Third, CBCs could have formed within the supernova fallback disk arising from the explosion (e.g., Wolszczan & Frail 1992). Note that fallback disks do not contain enough mass to enable star formation, but they do possess enough mass for the formation of substellar objects. Additional observations are needed to detect and characterize such disks (see Section 7.4).

On the other hand, stellar and substellar CBCs could be gravitationally captured by the X-ray binary. This is analogous to the case of the PSR B1620–26 system, where a giant exoplanet is thought to have been captured by a binary system containing an NS and a WD (e.g., Sigurdsson et al. 2003). Given that the HMXBs in our sample are massive ($>10\,M_\odot$) and located in the Galactic plane (see Figure 1), such events would not be unlikely.

7.4. Follow-up and Complementary Observations

The findings of our study primarily consist of intermediate results, and additional observations are necessary to conduct further analyses and confirm that the CBCs are bound to the system. In this section, we provide a list of recommendations for follow-up and complementary observations.

First, we recommend reobserving the systems in the same band (L') using the same instrument (NIRC2) at one or multiple additional epochs. This will allow us to conduct proper-motion analysis (see Section 6.2) for all the candidate CBCs identified in this study. Multiepoch observations will also enable us to characterize the orbital motion of these CBCs. Since the HMXBs presented in this study are located within 2–3 kpc, the time interval between epochs ranges from a few months to a few years. Table 4 provides an estimate of the recommended year of reobservation for each system, ensuring a statistically significant ($>3\sigma$) proper-motion analysis.

Second, we recommend observing the remaining five sources, such as Scorpius X-1, 1A 0620–00, and V404 Cyg, to complete the sample of all X-ray binaries within 2–3 kpc accessible with Keck/NIRC2. This would also enable us to incorporate LMXBs into the analysis and discussion.

Third, observations in other bands (e.g., K_s) would allow us to construct color–magnitude diagrams and employ evolutionary models to estimate the physical properties of the CBCs with greater constraints (e.g., Prasow-Émond et al. 2022). Similarly, obtaining the near-infrared spectrum of the candidate CBCs would enable us to characterize the nature of the source and extract additional physical properties. Finally, submillimeter observations of the continuum emission would allow us to detect

and characterize potential au-scale circumstellar or protoplanetary disks composed of dust and hot gas (e.g., Coleiro et al. 2013; Iyer & Paul 2017; Waisberg et al. 2019).

Contrast curves for all systems with CBCs can be found in the Appendix to assess the limit that has been reached during these observations.

8. Summary and Conclusions

In this study, we presented the first L'-band high-contrast images of nearby HMXBs using NIRC2 and the vortex coronagraph on the W. M. Keck Observatory. A total of 14 systems were observed from a sample of 19 X-ray binaries within ∼2–3 kpc and amenable for direct imaging. One or several sources with an S/N > 5 were found in eight of the observed X-ray binaries. To discern the nature of these sources —whether unrelated objects or candidate CBCs—we employed Galactic population models for all systems and proper-motion analysis for γ Cas. We find that, if confirmed, these results would imply the presence of stellar and substellar CBCs in the direct environment of X-ray binaries (∼350–12,000 au), which opens up the discussion on the binary nature of these systems. As a pilot study, this work presents a catalog of photometric and astrometric parameters for the first epochs of observations. Follow-up observations or additional characterization (e.g., infrared spectrum) will enable us to conduct proper-motion analyses to discriminate more robustly background/foreground sources from comoving, gravitationally bound CBCs.

Appendix

This appendix presents additional data related to the main text. Figure 6 presents the 5σ contrast curves for all X-ray binaries with CBCs. Table 5 presents additional relevant physical properties for the 14 observed X-ray binaries. Table 6 presents the properties of the detected sources in the high-contrast image, including the status (background/foreground source or candidate CBC), optimization parameters, physical properties (astrometric and photometric parameters), and estimated mass.
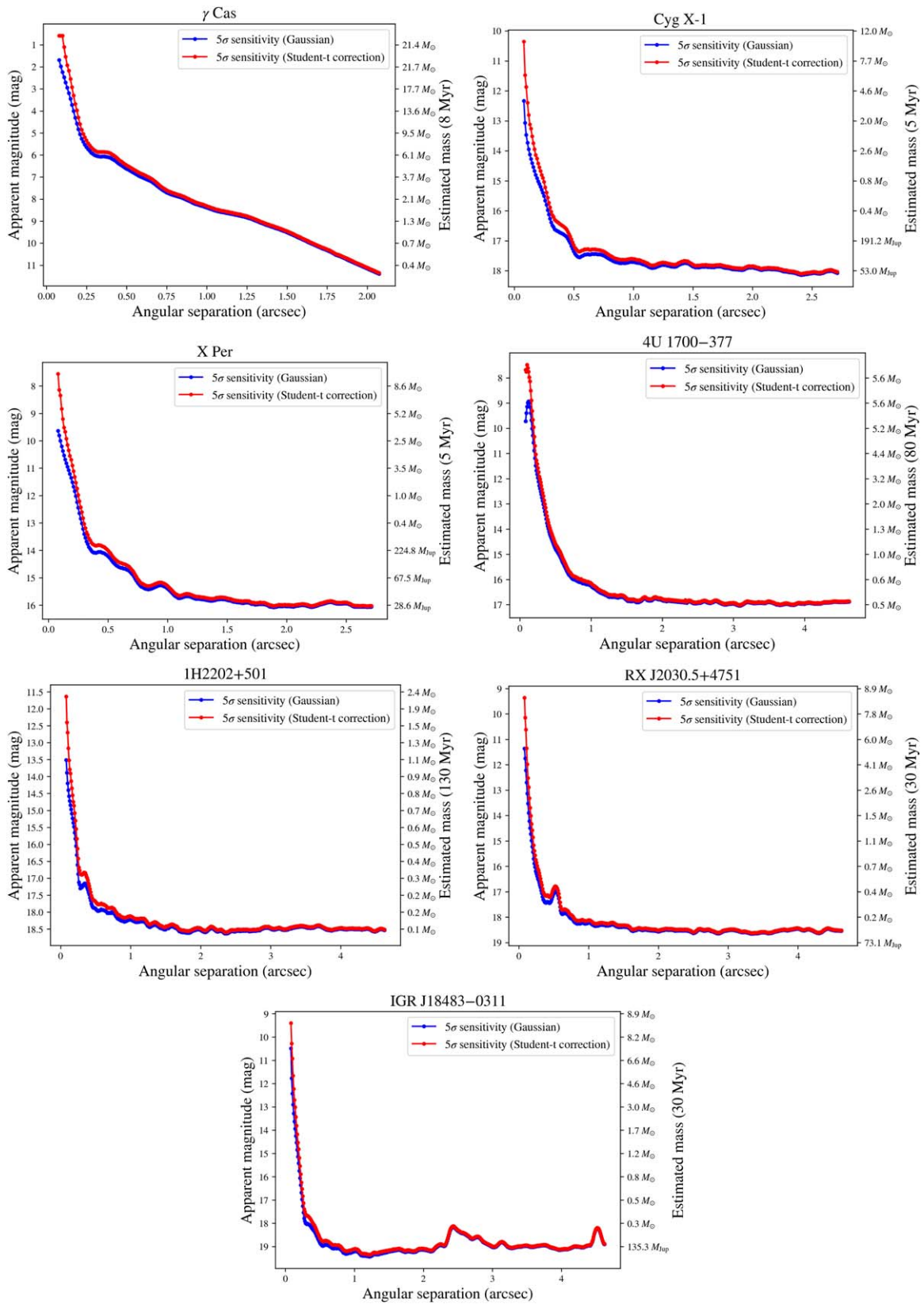
Figure 6. 5σ contrast curves in apparent magnitude (left axis) and estimated mass from the age of the X-ray binary (right axis) for γ Cas, Cyg X-1, X Per, 4U 1700 -377, 1H 2202+501, RX J2030.5+4751, and IGR J18483$-$0311. The curves were generated using VIP for a Gaussian distribution (blue) and with a Student's t-test correction (red).

Table 5
Additional Relevant Physical Properties for the 14 Observed X-Ray Binaries

Target	Distance (kpc)	PM R.A. (mas yr^{-1})	PM Decl. (mas yr^{-1})	m_L (±0.5 mag)	Age (Myr)	$E(B-V)$	References	L_X (erg s^{-1})	References	Var. Ind.
(1)	(2)	(3)	(4)	(5)	(6)	(7)	(8)	(9)	(10)	(11)
RX J1744.7−2713	1.22 ± 0.04	-0.87 ± 0.02	-2.30 ± 0.02	5.809	Up to ∼60	∼3.4	(1)	$(3.08 \pm 0.49)\times10^{32}$	(2)	N/A
IGR J18483−0311	2.6 ± 0.7	-1.7 ± 0.2	-3.7 ± 0.1	7.907	Up to ∼30–50	5.22 ± 0.02	(3)	From ∼10^{33} to 10^{36}	(3, 4, 5)	N
γ Cas	0.19 ± 0.02	25.7 ± 0.5	-3.8 ± 0.4	−0.912	8.0 ± 0.4	−0.15	(6)	∼10^{32}–10^{33}	(7)	N
SAX J1818.6−1703	2.3 ± 0.8	-1.6 ± 0.2	-4.6 ± 0.1	8.964	Up to ∼30–50	5.08 ± 0.05	(3)	From ∼10^{32} to 10^{35}	(3, 8)	Y
1H 2202+501	1.10 ± 0.01	2.36 ± 0.01	-0.29 ± 0.01	8.285	Up to ∼130	0.36 ± 0.03	(9)	∼9×10^{32}	(10)	N/A
4U 2206+543	3.1 ± 0.1	-4.17 ± 0.02	-3.32 ± 0.01	8.700	Up to ∼8	0.547 ± 0.066	(11)	∼10^{35}–10^{36}	(12, 13)	N
4U 1700−377	1.5 ± 0.1	2.41 ± 0.03	5.02 ± 0.02	5.36	∼80	0.50 ± 0.01	(14)	Up to ∼7×10^{36}	(15)	N
IGR J17544−2619	2.4 ± 0.2	-0.51 ± 0.03	-0.67 ± 0.02	7.67	Up to ∼8	N/A		From ∼10^{32} to 10^{38}	(16, 17)	Y
RX J2030.5+4751	2.30 ± 0.07	-2.71 ± 0.02	-4.54 ± 0.02	7.088	Up to ∼30–50	N/A		Up to∼10^{33}	(18, 19)	N/A
Cyg X-1	2.1 ± 0.1	-3.81 ± 0.01	-6.31 ± 0.02	6.406	5 ± 1.5	1.11 ± 0.03	(20)	∼3×10^{37}	(21)	N
X Per	0.6 ± 0.1	-1.28 ± 0.05	-1.87 ± 0.03	4.596	∼5	∼0.4	(22)	∼4×10^{34}	(23)	N
1H 0556+286	1.5 ± 0.1	0.63 ± 0.03	-2.19 ± 0.02	7.618	Up to ∼150	N/A		Up to ∼4×10^{35}	(24)	N/A
RX J0648.1−4419	0.52 ± 0.01	-4.16 ± 0.07	5.93 ± 0.06	9.150	N/A	N/A		∼10^{32}	(25)	N/A
Vela X-1	2.0 ± 0.1	-4.82 ± 0.02	9.28 ± 0.02	5.458	Up to ∼30–50	∼0.8	(26)	Up to ∼4×10^{36}	(27)	N

Note. Column (1): name of the target. Column (2): distance in kpc (see Section 3.3.1). Column (3): proper motion in R.A. in mas yr^{-1}. Column (4): proper motion in decl. in mas yr^{-1}. Column (5): apparent magnitude in the L' band (see Section 3.3.2). Column (6): estimated age of the X-ray binary in Myr (see Section 3.3.3). Column (7): value of the extinction. Column (8): reference for the extinction. Column (9): observed values of the X-ray luminosity in erg s^{-1}. Column (10): reference for the X-ray luminosity. Column (11): the variability indicator, as found in Bird et al. (2016).

References. (1) Schlafly & Finkbeiner 2011; (2) Naze & Motch 2018; (3) Torrejón et al. 2010; (4) Romano et al. 2010; (5) Sguera et al. 2015; (6) Moffat et al. 1973; (7) Raguzova & Popov 2005; (8) Bozzo et al. 2012; (9) Simon et al. 2019; (10) Chevalier & Ilovaisky 1998; (11) Nikolov et al. 2017; (12) Negueruela & Reig 2001; (13) Ribó et al. 2006; (14) Hainich et al. 2020; (15) Laurent et al. 1992; (16) Romano et al. 2015; (17) Bozzo et al. 2016; (18) Liu et al. 2006; (19) Raguzova 2007; (20) Caballero-Nieves et al. 2009; (21) Di Salvo et al. 2001; (22) Lyubimkov et al. 1997; (23) Coburn et al. 2001; (24) Helfand & Moran 2001; (25) Mereghetti et al. 2021; (26) Klare & Neckel 1977; (27) Kreykenbohm et al. 2008.

Table 6
Physical Properties of the Detected Sources in the High-contrast Images

Target	Source (S/N > 5)	Status	n_{comp}	$n_{foV}(\mathcal{L}' \leqslant m_{L'})$	$1 - P_{unrelated}(\Sigma, \Theta)$ (%)	ρ (mas)	θ (deg)	$m_{L'}$ (mag)	Est. Mass	Proj. Sep. (au)
(1)	(2)	(3)	(4)	(5)	(6)	(7)	(8)	(9)	(10)	(11)
X Per	B	cc	20	∼0.1	> 99	587 ± 18	112.3 ± 2.0	14.4 ± 0.6	∼45M_{Jup}−110M_{Jup}	350
Cyg X-1	B	cc	26	∼0.6	93 ± 1	1853 ± 12	170.1 ± 0.6	16.2 ± 0.6	∼0.2–0.3 $M_\odot$	4000
IGR J18483−0311	B	cc	2	0.3−0.8	90 ± 4	2527 ± 12	291.5 ± 0.2	13.3 ± 0.8	∼2.5 $M_\odot$	6440
	C	cc	3	0.9−1.8	89 ± 4	1516 ± 13	21.6 ± 0.4	14.8 ± 0.8	∼1.1–1.3 $M_\odot$	3865
	D	bkg	7	3.4−7.0	32 ± 15	2787 ± 14	16.9 ± 0.2	16.3 ± 0.8	⋯	7100
	E	bkg	13	4.1−8.3	14 ± 10	3127 ± 15	13.8 ± 0.2	16.7 ± 0.8	⋯	7975
	F	bkg	17	1.3−3.1	23 ± 10	4522 ± 14	15.0 ± 0.1	15.3 ± 0.8	⋯	11530
	G	bkg	25	∼7	<5	3761 ± 12	69.7 ± 0.2	17.0 ± 0.8	⋯	9600
	H	bkg	23	∼11	<5	3358 ± 13	83.3 ± 0.2	17.6 ± 0.8	⋯	8560
	I	bkg	19	∼11	<5	3168 ± 15	106.8 ± 0.2	17.6 ± 0.8	⋯	8080
SAX J1818.6−1703	B	bkg	3	1.5−3.5	25 ± 10	2820 ± 11	96.9 ± 0.2	18.2 ± 0.8	⋯	6600
	C	bkg	20	> 30	<5	4069 ± 12	353.9 ± 0.2	14.9 ± 0.8	⋯	9525
1H 2202+501	B	cc	14	0.2−0.5	98 ± 1	1222 ± 15	162.4 ± 0.5	16.4 ± 0.9	∼70M_{Jup} to ∼0.4 $M_\odot$	1370
4U 1700−377	B	cc	8	0.5−0.7	91 ± 3	2238 ± 12	353.0 ± 0.3	14.0 ± 0.6	∼1.2–1.3 $M_\odot$	4075
	C	cc	7	1.3−1.9	68 ± 4	2616 ± 12	274.4 ± 0.2	13.4 ± 0.6	∼1.5–1.6 $M_\odot$	4760
	D	cc	3	0.7−0.9	65 ± 6	4157 ± 15	283.4 ± 0.1	15.4 ± 0.7	∼0.4–0.8 $M_\odot$	7570
IGR J17544−2619	B	bkg	5	∼48	<5	827 ± 12	19.4 ± 0.7	16.9 ± 0.8	⋯	2350
	C	bkg	12	∼13	<5	2993 ± 13	10.8 ± 0.2	15.1 ± 0.8	⋯	8500
	D	bkg	3	∼6	<5	4099 ± 11	72.5 ± 0.1	13.4 ± 0.8	⋯	11640
	E	bkg	15	∼86	<5	3170 ± 14	70.7 ± 0.2	17.3 ± 0.8	⋯	9000
	F	bkg	11	∼14	∼7	2392 ± 14	103.5 ± 0.2	15.3 ± 0.8	⋯	6790
	G	bkg	3	∼22	<5	2947 ± 12	118.7 ± 0.2	16.1 ± 0.8	⋯	8370
	H	bkg	8	∼8	<5	3935 ± 13	147.7 ± 0.1	14.1 ± 0.8	⋯	11180
	I	bkg	10	∼68	<5	2093 ± 11	235.1 ± 0.3	17.1 ± 0.8	⋯	5950
	J	bkg	15	∼85	<5	3537 ± 15	267.1 ± 0.2	17.3 ± 0.8	⋯	10050
RX J2030.5+4751	B	cc	7	∼0.1	> 99	513 ± 11	302.9 ± 0.9	14.8 ± 0.8	∼0.3–1.1 $M_\odot$	1130
	C	cc	17	0.2−0.3	92 ± 3	3251 ± 15	132.1 ± 0.3	16.1 ± 0.8	∼0.1–0.6 $M_\odot$	7150
	D	cc	28	0.3−0.7	74 ± 8	4208 ± 13	343.1 ± 0.3	17.1 ± 0.8	∼60M_{Jup}−400M_{Jup}	9250
γ Cas (2017)	B	⋯	1	⋯	⋯	2051 ± 20	242.8 ± 0.3	⋯	⋯	390
	C	⋯	24	⋯	⋯	1803 ± 20	91.4 ± 0.3	⋯	⋯	343
γ Cas (2020)	B	cc	1	⋯	⋯	2056 ± 20	241.2 ± 0.3	3.1 ± 0.9	∼13 $M_\odot$	391
	C	bkg	24	⋯	⋯	1721 ± 20	90.8 ± 0.3	10.4 ± 0.9	⋯	327

Note. Column (1): the target. Column (2): the label of the detected source (S/N > 5). Column (3): the current status of the source, either background/foreground object (bkg) or candidate CBC (cc). Column (4): the optimal number of principal components used for the fitting (n_{comp}). Column (5): the expected number of sources in the FOV below the apparent magnitude ($n_{FOV}(\mathcal{L}' \leqslant m_{L'})$); see Section 6.1. Column (6): one minus the probability of being unrelated with the central X-ray binary ($1 - P_{unrelated}(\Sigma, \Theta)$; see Section 6.1). Column (7): the radial separation from the X-ray binary in mas. Column (8): the position angle in the image in degrees. Column (9): the apparent magnitude in the L' band (no extinction correction was applied). Column (10): the mass of the source, in $M_\odot$ or M_{Jup}, estimated from evolutionary models (MIST or COND/DUSTY). Column (11): the projected separation from the X-ray binary in astronomical units.

ORCID iDs

M. Prasow-Émond ⬤ https://orcid.org/0000-0002-2457-3431
J. Hlavacek-Larrondo ⬤ https://orcid.org/0000-0001-7271-7340
K. Fogarty ⬤ https://orcid.org/0000-0002-2691-2476
É. Artigau ⬤ https://orcid.org/00000-0003-3506-5667
D. Mawet ⬤ https://orcid.org/0000-0002-8895-4735
P. Gandhi ⬤ https://orcid.org/0000-0003-3105-2615
J. F. Steiner ⬤ https://orcid.org/0000-0002-5872-6061
J. Rameau ⬤ https://orcid.org/0000-0003-0029-0258
D. Lafrenière ⬤ https://orcid.org/0000-0002-6780-4252
A. Fabian ⬤ https://orcid.org/0000-0002-9378-4072
D. J. Walton ⬤ https://orcid.org/0000-0001-5819-3552
R. Doyon ⬤ https://orcid.org/0000-0001-5485-4675
B. B. Ren (任彬) ⬤ https://orcid.org/0000-0003-1698-9696

References

Abate, C., Pols, O. R., Izzard, R. G., Mohamed, S. S., & de Mink, S. E. 2013, A&A, 552, A26
Avakyan, A., Neumann, M., Zainab, A., et al. 2023, A&A, 675, A199
Bailer-Jones, C. A. L., Rybizki, J., Fouesneau, M., Demleitner, M., & Andrae, R. 2021, AJ, 161, 147
Bakos, G. Á., Noyes, R. W., Kovács, G., et al. 2007, ApJ, 656, 552
Bala, S., Roy, J., & Bhattacharya, D. 2020, MNRAS, 493, 3045
Bate, M. R. 2012, MNRAS, 419, 3115
Belczynski, K., & Ziolkowski, J. 2009, ApJ, 707, 870
Bhalerao, V., Romano, P., Tomsick, J., et al. 2015, MNRAS, 447, 2274
Bikmaev, I. F., Nikolaeva, E. A., Shimansky, V. V., et al. 2017, AstL, 43, 664
Bird, A. J., Barlow, E. J., Bassani, L., et al. 2004, ApJL, 607, L33
Bird, A. J., Bazzano, A., Hill, A. B., et al. 2009, MNRAS, 393, L11
Bird, A. J., Bazzano, A., Malizia, A., et al. 2016, ApJS, 223, 15
Bird, A. J., Malizia, A., Bazzano, A., et al. 2007, ApJS, 170, 175
Blackman, J. W., Beaulieu, J. P., Bennett, D. P., et al. 2021, Natur, 598, 272
Blay, P., Ribó, M., Negueruela, I., et al. 2005, A&A, 438, 963
Bohn, A. J., Ginski, C., Kenworthy, M. A., et al. 2021, A&A, 648, A73
Bolton, C. T. 1972a, NPhS, 240, 124
Bolton, C. T. 1972b, Natur, 235, 271
Bonavita, M., Desidera, S., Thalmann, C., et al. 2016, A&A, 593, A38
Bond, C. Z., Wizinowich, P., Chun, M., et al. 2018, Proc. SPIE, 10703, 107031Z
Boon, C. M., Bird, A. J., Hill, A. B., et al. 2016, MNRAS, 456, 4111
Boroson, B., Vrtilek, S. D., Kallman, T., & Corcoran, M. 2003, ApJ, 592, 516
Bozzo, E., Bhalerao, V., Pradhan, P., et al. 2016, A&A, 596, A16
Bozzo, E., Pavan, L., Ferrigno, C., et al. 2012, A&A, 544, A118
Brandeker, A., Jayawardhana, R., Khavari, P., Haisch, K. E., & Mardones, D. 2006, ApJ, 652, 1572
Burrows, A., Hubbard, W. B., Lunine, J. I., & Liebert, J. 2001, RvMP, 73, 719
Caballero-Nieves, S. M., Gies, D. R., Bolton, C. T., et al. 2009, ApJ, 701, 1895
Charles, P. A., & Coe, M. J. 2006, Compact Stellar X-Ray Sources (Cambridge: Cambridge Univ. Press), 215
Charles, P. A., Mason, K. O., White, N. E., et al. 1978, MNRAS, 183, 813
Chaty, S., Rahoui, F., Foellmi, C., et al. 2008, A&A, 484, 783
Chen, W.-C., & Podsiadlowski, P. 2016, ApJ, 830, 131
Chernyakova, M., Lutovinov, A., Capitanio, F., Lund, N., & Gehrels, N. 2003, ATel, 157, 1
Chevalier, C., & Ilovaisky, S. A. 1998, A&A, 330, 201
Chini, R., Hoffmeister, V. H., Nasseri, A., Stahl, O., & Zinnecker, H. 2012, MNRAS, 424, 1925
Choi, J., Dotter, A., Conroy, C., et al. 2016, ApJ, 823, 102
Chun, S.-H., Jung, M., Kang, M., Kim, J.-W., & Sohn, Y.-J. 2015, A&A, 578, A51
Coburn, W., Heindl, W. A., Gruber, D. E., et al. 2001, ApJ, 552, 738
Coburn, W., Heindl, W. A., Rothschild, R. E., et al. 2002, ApJ, 580, 394
Coleiro, A., & Chaty, S. 2013, ApJ, 764, 185
Coleiro, A., Chaty, S., Zurita Heras, J. A., Rahoui, F., & Tomsick, J. A. 2013, A&A, 560, A108
Corbet, R. H. D., Markwardt, C. B., & Tueller, J. 2007, ApJ, 655, 458
Corbet, R. H. D., & Peele, A. G. 2001, ApJ, 562, 936
Correia, S., Zinnecker, H., Ratzka, T., & Sterzik, M. F. 2006, A&A, 459, 909
De Angeli, F., Weiler, M., Montegriffo, P., et al. 2023, A&A, 674, A2

Delgado-Martí, H., Levine, A. M., Pfahl, E., & Rappaport, S. A. 2001, ApJ, 546, 455
Desidera, S., & Barbieri, M. 2007, A&A, 462, 345
Di Salvo, T., Done, C., Życki, P. T., Burderi, L., & Robba, N. R. 2001, ApJ, 547, 1024
Dietrich, J., & Ginski, C. 2018, A&A, 620, A102
Diez, C. M., Grinberg, V., Fürst, F., et al. 2022, A&A, 660, A19
Done, C., Gierliński, M., & Kubota, A. 2007, A&ARv, 15, 1
Doroshenko, V., Santangelo, A., Kreykenbohm, I., & Doroshenko, R. 2012, A&A, 540, L1
Dotter, A. 2016, ApJS, 222, 8
Drave, S. P., Bird, A. J., Sidoli, L., et al. 2014, MNRAS, 439, 2175
Drave, S. P., Bird, A. J., Townsend, L. J., et al. 2012, A&A, 539, A21
Ducci, L., Doroshenko, V., Sasaki, M., et al. 2013, A&A, 559, A135
Ducci, L., Romano, P., Ji, L., & Santangelo, A. 2019, A&A, 631, A135
Duchêne, G., & Kraus, A. 2013, ARA&A, 51, 269
Dupree, A. K., Davis, R. J., Gursky, H., et al. 1978, Natur, 275, 400
Eggleton, P. P., & Tokovinin, A. A. 2008, MNRAS, 389, 869
El Mellah, I., Sundqvist, J. O., & Keppens, R. 2019, A&A, 622, L3
Eriksson, S. C., Asensio Torres, R., Janson, M., et al. 2020, A&A, 638, L6
Esin, A. A., Narayan, R., Cui, W., Grove, J. E., & Zhang, S.-N. 1998, ApJ, 505, 854
Fabian, A. C., Rees, M. J., Stella, L., & White, N. E. 1989, MNRAS, 238, 729
Faherty, J. K., Riedel, A. R., Cruz, K. L., et al. 2016, ApJS, 225, 10
Fender, R. P., Belloni, T. M., & Gallo, E. 2004, MNRAS, 355, 1105
Finger, M. H., Ikhsanov, N. R., Wilson-Hodge, C. A., & Patel, S. K. 2010, ApJ, 709, 1249
Franson, K., Bowler, B. P., Brandt, T. D., et al. 2022, AJ, 163, 50
Fürst, F., Pottschmidt, K., Wilms, J., et al. 2014, ApJ, 780, 133
Gandhi, P., Buckley, D. A. H., Charles, P. A., et al. 2022, MNRAS, 510, 3885
Giacconi, R., Kellogg, E., Gorenstein, P., Gursky, H., & Tananbaum, H. 1971, ApJL, 165, L27
Giacconi, R., Murray, S., Gursky, H., et al. 1972, ApJ, 178, 281
Giménez-García, A., Shenar, T., Torrejón, J. M., et al. 2016, A&A, 591, A26
Giménez-García, A., Torrejón, J. M., Eikmann, W., et al. 2015, A&A, 576, A108
Girardi, L., Groenewegen, M. A. T., Hatziminaoglou, E., & da Costa, L. 2005, A&A, 436, 895
Gomez Gonzalez, C. A., Wertz, O., Absil, O., et al. 2017, AJ, 154, 7
González-Riestra, R., Oosterbroek, T., Kuulkers, E., Orr, A., & Parmar, A. N. 2004, A&A, 420, 589
Grebenev, S. A., Lutovinov, A. A., & Sunyaev, R. A. 2003, ATel, 192, 1
Grebenev, S. A., Rodriguez, J., Westergaard, N. J., Sunyaev, R. A., & Oosterbroek, T. 2004, ATel, 252, 1
Grebenev, S. A., & Sunyaev, R. A. 2005, AstL, 31, 672
Haberl, F., White, N. E., & Kallman, T. R. 1989, ApJ, 343, 409
Hainich, R., Oskinova, L. M., Torrejón, J. M., et al. 2020, A&A, 634, A49
Hanson, M. M., Conti, P. S., & Rieke, M. J. 1996, ApJS, 107, 281
Hawkins, F. J., Mason, K. O., & Sanford, P. W. 1975, ApL, 16, 19
Helfand, D. J., & Moran, E. C. 2001, ApJ, 554, 27
Hiltner, W. A., Werner, J., & Osmer, P. 1972, ApJL, 175, L19
Huby, E., Bottom, M., Femenia, B., et al. 2017, A&A, 600, A46
Hutter, D. J., Tycner, C., Zavala, R. T., et al. 2021, ApJS, 257, 69
Ikhsanov, N. R., & Beskrovnaya, N. G. 2010, Ap, 53, 237
Imara, N., & Di Stefano, R. 2018, ApJ, 859, 40
in 't Zand, J., Heise, J., Smith, M., et al. 1998, IAUC, 6840, 2
in 't Zand, J., Jonker, P., Mendez, M., & Markwardt, C. 2006, ATel, 915, 1
in 't Zand, J. J. M. 2005, A&A, 441, L1
Israel, G. L., Stella, L., Angelini, L., et al. 1997, ApJL, 474, L53
Iyer, N., & Paul, B. 2017, MNRAS, 471, 355
Jaschek, M., & Jaschek, C. 1963, PASP, 75, 365
Jones, C., Forman, W., Tananbaum, H., et al. 1973, ApJL, 181, L43
Jones, C., Nally, C., Sharp, M. J., et al. 2021, MNRAS, 504, 565
Justham, S., Rappaport, S., & Podsiadlowski, P. 2006, MNRAS, 366, 1415
Kara, E., Steiner, J. F., Fabian, A. C., et al. 2019, Natur, 565, 198
Khargharia, J., Froning, C. S., & Robinson, E. L. 2010, ApJ, 716, 1105
Kiseleva, G., Eggleton, P. P., & Anosova, J. P. 1994, MNRAS, 267, 161
Klare, G., & Neckel, T. 1977, A&AS, 27, 215
Kratter, K. M., Matzner, C. D., Krumholz, M. R., & Klein, R. I. 2010, ApJ, 708, 1585
Kravtsov, V., Berdyugin, A. V., Piirola, V., et al. 2020, A&A, 643, A170
Kretschmar, P., El Mellah, I., Martínez-Núñez, S., et al. 2021, A&A, 652, A95
Kreykenbohm, I., Coburn, W., Wilms, J., et al. 2002, A&A, 395, 129
Kreykenbohm, I., Wilms, J., Kretschmar, P., et al. 2008, A&A, 492, 511
Krimm, H. A., Holland, S. T., Corbet, R. H. D., et al. 2013, ApJS, 209, 14
Kubo, S., Murakami, T., Ishida, M., & Corbet, R. H. D. 1998, PASJ, 50, 417
Kuulkers, E., Oneca, D. R., Brandt, S., et al. 2007, ATel, 1266, 1

La Barbera, A., Santangelo, A., Orlandini, M., & Segreto, A. 2003, A&A, 400, 993

La Palombara, N., Esposito, P., Mereghetti, S., Novara, G., & Tiengo, A. 2015, A&A, 580, A56

La Palombara, N., & Mereghetti, S. 2007, A&A, 474, 137

Lafrenière, D., Jayawardhana, R., Brandeker, A., Ahmic, M., & van Kerkwijk, M. H. 2008, ApJ, 683, 844

Lafrenière, D., Jayawardhana, R., van Kerkwijk, M. H., Brandeker, A., & Janson, M. 2014, ApJ, 785, 47

Lagrange, A. M., Bonnefoy, M., Chauvin, G., et al. 2010, Sci, 329, 57

Laurent, P., Goldwurm, A., Lebrun, F., et al. 1992, A&A, 260, 237

Liu, Q. Z., Chaty, S., & Yan, J. Z. 2011, MNRAS, 415, 3349

Liu, Q. Z., van Paradijs, J., & van den Heuvel, E. P. J. 2000, A&AS, 147, 25

Liu, Q. Z., van Paradijs, J., & van den Heuvel, E. P. J. 2006, A&A, 455, 1165

Liu, Q. Z., van Paradijs, J., & van den Heuvel, E. P. J. 2007, A&A, 469, 807

Lopes de Oliveira, R., Motch, C., Haberl, F., Negueruela, I., & Janot-Pacheco, E. 2006, A&A, 454, 265

Lutovinov, A., Revnivtsev, M., Gilfanov, M., et al. 2005, A&A, 444, 821

Lutovinov, A., Tsygankov, S., & Chernyakova, M. 2012, MNRAS, 423, 1978

Lyubimkov, L. S., Rostopchin, S. I., Roche, P., & Tarasov, A. E. 1997, MNRAS, 286, 549

Maitra, C., Raichur, H., Pradhan, P., & Paul, B. 2017, MNRAS, 470, 713

Markoff, S., Falcke, H., & Fender, R. 2001, A&A, 372, L25

Marois, C., Lafrenière, D., Doyon, R., Macintosh, B., & Nadeau, D. 2006, ApJ, 641, 556

Martin, R. G., Pringle, J. E., Tout, C. A., & Lubow, S. H. 2011, MNRAS, 416, 2827

Martínez-Chicharro, M., Grinberg, V., Torrejón, J. M., et al. 2021, MNRAS, 501, 5646

Martínez-Núñez, S., Torrejón, J. M., Kühnel, M., et al. 2014, A&A, 563, A70

Masetti, N., Dal Fiume, D., Amati, L., et al. 2004, A&A, 423, 311

Mason, K. O., White, N. E., Sanford, P. W., et al. 1976, MNRAS, 176, 193

Mastroserio, G., Ingram, A., & van der Klis, M. 2019, MNRAS, 488, 348

Mawet, D., Riaud, P., Absil, O., & Surdej, J. 2005, ApJ, 633, 1191

Mereghetti, S., La Palombara, N., Tiengo, A., et al. 2011, ApJ, 737, 51

Mereghetti, S., Pintore, F., Esposito, P., et al. 2016, MNRAS, 458, 3523

Mereghetti, S., Pintore, F., Rauch, T., et al. 2021, MNRAS, 504, 920

Mereghetti, S., Tiengo, A., Esposito, P., et al. 2009, Sci, 325, 1222

Miller-Jones, J. C. A., Bahramian, A., Orosz, J. A., et al. 2021, Sci, 371, 1046

Mirabel, I. F., & Rodrigues, I. 2003, Sci, 300, 1119

Moffat, A. F. J., Haupt, W., & Schmidt-Kaler, T. 1973, A&A, 23, 433

Mohamed, S., & Podsiadlowski, P. 2007, in ASP Conf. Ser. 372, 15th European Workshop on White Dwarfs, ed. R. Napiwotzki & M. R. Burleigh (San Francisco, CA: ASP), 397

Montegriffo, P., De Angeli, F., Andrae, R., et al. 2023, A&A, 674, A3

Mooley, K. P., Nakar, E., Hotokezaka, K., et al. 2018, Natur, 554, 207

Motch, C., Haberl, F., Dennerl, K., Pakull, M., & Janot-Pacheco, E. 1997, A&A, 323, 853

Murdin, P., & Webster, B. L. 1971, Natur, 233, 110

Naud, M.-E., Artigau, É., Malo, L., et al. 2014, ApJ, 787, 5

Naze, Y., & Motch, C. 2018, A&A, 619, A148

Negueruela, I., & Reig, P. 2001, A&A, 371, 1056

Negueruela, I., & Smith, D. M. 2006, ATel, 831, 1

Negueruela, I., Smith, D. M., Reig, P., Chaty, S., & Torrejón, J. M. 2006, in The X-ray Universe 2005, ed. A. Wilson (Noordwijk: ESA), 165

Nemravová, J., Harmanec, P., Koubský, P., et al. 2012, A&A, 537, A59

Neumann, M., Avakyan, A., Doroshenko, V., & Santangelo, A. 2023, A&A, 677, A134

Nikolov, Y. M., Zamanov, R. K., Stoyanov, K. A., & Martí, J. 2017, BlgAJ, 27, 10

Okazaki, A. T., Bate, M. R., Ogilvie, G. I., & Pringle, J. E. 2002, MNRAS, 337, 967

Orosz, J. A., McClintock, J. E., Aufdenberg, J. P., et al. 2011, ApJ, 742, 84

Paczyński, B. 1967, AcA, 17, 287

Parker, M. L., Tomsick, J. A., Miller, J. M., et al. 2015, ApJ, 808, 9

Paxton, B., Bildsten, L., Dotter, A., et al. 2011, ApJS, 192, 3

Paxton, B., Cantiello, M., Arras, P., et al. 2013, ApJS, 208, 4

Paxton, B., Marchant, P., Schwab, J., et al. 2015, ApJS, 220, 15

Paxton, B., Schwab, J., Bauer, E. B., et al. 2018, ApJS, 234, 34

Pellizza, L. J., Chaty, S., & Negueruela, I. 2006, A&A, 455, 653

Perryman, M. A. C., Lindegren, L., Kovalevsky, J., et al. 1997, A&A, 323, L49

Peter, D., Feldt, M., Henning, T., & Hormuth, F. 2012, A&A, 538, A74

Popov, S. B., Mereghetti, S., Blinnikov, S. I., Kuranov, A. G., & Yungelson, L. R. 2018, MNRAS, 474, 2750

Popper, D. M. 1950, ApJ, 111, 495

Postnov, K., Oskinova, L., & Torrejón, J. M. 2017, MNRAS, 465, L119

Prasow-Émond, M., Hlavacek-Larrondo, J., Fogarty, K., et al. 2022, AJ, 164, 7

Raguzova, N. V. 2007, BeSN, 38, 24

Raguzova, N. V., & Popov, S. B. 2005, A&AT, 24, 151

Rahoui, F., & Chaty, S. 2008, A&A, 492, 163

Rampy, R. A., Smith, D. M., & Negueruela, I. 2009, ApJ, 707, 243

Reig, P., Torrejón, J. M., Negueruela, I., et al. 2009, A&A, 494, 1073

Reynolds, A. P., Owens, A., Kaper, L., Parmar, A. N., & Segreto, A. 1999, A&A, 349, 873

Ribó, M., Negueruela, I., Blay, P., Torrejón, J. M., & Reig, P. 2006, A&A, 449, 687

Rímulo, L. R., Carciofi, A. C., Vieira, R. G., et al. 2018, MNRAS, 476, 3555

Robinson, R. D., & Smith, M. A. 2000, ApJ, 540, 474

Romano, P., Bozzo, E., Mangano, V., et al. 2015, A&A, 576, L4

Romano, P., Sidoli, L., Ducci, L., et al. 2010, MNRAS, 401, 1564

Rubin, B. C., Finger, M. H., Harmon, B. A., et al. 1996, ApJ, 459, 259

Saraswat, P., & Apparao, K. M. V. 1992, ApJ, 401, 678

Sarty, G. E., Pilecki, B., Reichart, D. E., et al. 2011, RAA, 11, 947

Savonije, G. J. 1978, A&A, 62, 317

Schlafly, E. F., & Finkbeiner, D. P. 2011, ApJ, 737, 103

Sell, P. H., Heinz, S., Richards, E., et al. 2015, MNRAS, 446, 3579

Serabyn, E., Liewer, K., & Mawet, D. 2016, OptCo, 379, 64

Service, M., Lu, J. R., Campbell, R., et al. 2016, PASP, 128, 095004

Servillat, M., Tang, S., Grindlay, J. E., & Los, E. 2012, Proc. "An INTEGRAL View of the High-energy Sky (the First 10 years)"—9th INTEGRAL Workshop and Celebration of the 10th Anniversary of the Launch (INTEGRAL 2012) (Trieste: SISSA), 23, http://pos.sissa.it/cgi-bin/reader/conf.cgi?confid=176

Seto, N. 2018, MNRAS, 475, 1392

Sguera, V., Barlow, E. J., Bird, A. J., et al. 2005, A&A, 444, 221

Sguera, V., Ducci, L., Sidoli, L., Bazzano, A., & Bassani, L. 2010, MNRAS, 402, L49

Sguera, V., Hill, A. B., Bird, A. J., et al. 2007, A&A, 467, 249

Sguera, V., Sidoli, L., Bird, A. J., & Bazzano, A. 2015, MNRAS, 449, 1228

Shrader, C. R., Hamaguchi, K., Sturner, S. J., et al. 2015, ApJ, 799, 84

Sidoli, L. 2012, Proc. "An INTEGRAL view of the high-energy sky (the first 10 years)" - 9th INTEGRAL Workshop and celebration of the 10th anniversary of the launch (INTEGRAL 2012) (Trieste: SISSA), http://pos.sissa.it/cgi-bin/reader/conf.cgi?confid=176

Sidoli, L., Paizis, A., & Postnov, K. 2016, MNRAS, 457, 3693

Sidoli, L., Romano, P., Esposito, P., et al. 2009, MNRAS, 400, 258

Sigurdsson, S., Richer, H. B., Hansen, B. M., Stairs, I. H., & Thorsett, S. E. 2003, Sci, 301, 193

Simon, A. O., Metlova, N. V., Godunova, V. G., & Vasylenko, V. V. 2019, KPCB, 35, 38

Smith, D. M., Markwardt, C. B., Swank, J. H., & Negueruela, I. 2012, MNRAS, 422, 2661

Sota, A., Maíz Apellániz, J., Morrell, N. I., et al. 2014, ApJS, 211, 10

Sota, A., Maíz Apellániz, J., Walborn, N. R., et al. 2011, ApJS, 193, 24

Spiewak, R., Bailes, M., Barr, E. D., et al. 2018, MNRAS, 475, 469

Steele, I. A. 2016a, ATel, 8927, 1

Steele, I. A. 2016b, ATel, 9265, 1

Steele, I. A. 2016c, ATel, 9487, 1

Steele, I. A., Negueruela, I., & Clark, J. S. 1999, A&AS, 137, 147

Steiner, J. E., Ferrara, A., Garcia, M., et al. 1984, ApJ, 280, 688

Strohmayer, T. E. 2002, ApJ, 581, 577

Sunyaev, R. A., Grebenev, S. A., Lutovinov, A. A., et al. 2003, ATel, 190, 1

Tauris, T. M., & van den Heuvel, E. P. J. 2006, in Compact Stellar X-ray Sources, ed. W. Lewin & M. van der Klis (Cambridge: Cambridge Univ. Press), 623

Tetarenko, B. E., Shaw, A. W., Manrow, E. R., et al. 2021, MNRAS, 501, 3406

Tomsick, J. A., Nowak, M. A., Parker, M., et al. 2014, ApJ, 780, 78

Torrejón, J. M., Kreykenbohm, I., Orr, A., Titarchuk, L., & Negueruela, I. 2004, A&A, 423, 301

Torrejón, J. M., Negueruela, I., Smith, D. M., & Harrison, T. E. 2010, A&A, 510, A61

Torrejón, J. M., & Orr, A. 2001, A&A, 377, 148

Torrejón, J. M., Reig, P., Fürst, F., et al. 2018, MNRAS, 479, 3366

Valencic, L. A., & Smith, R. K. 2013, ApJ, 770, 22

Van, K. X., Ivanova, N., & Heinke, C. O. 2019, MNRAS, 483, 5595

van der Klis, M., & Bonnet-Bidaud, J. M. 1984, A&A, 135, 155

van der Meer, A., Kaper, L., di Salvo, T., et al. 2005, A&A, 432, 999

van der Meij, V., Guo, D., Kaper, L., & Renzo, M. 2021, A&A, 655, A31

van Kerkwijk, M. H., van Paradijs, J., Zuiderwijk, E. J., et al. 1995, A&A, 303, 483

Vanderburg, A., Rappaport, S. A., Xu, S., et al. 2020, Natur, 585, 363

Verbunt, F., & Zwaan, C. 1981, A&A, 100, L7
Waisberg, I., Dexter, J., Petrucci, P.-O., Dubus, G., & Perraut, K. 2019, A&A, 623, A47
Walter, R., & Zurita Heras, J. 2007, A&A, 476, 335
Walton, D. J., Tomsick, J. A., Madsen, K. K., et al. 2016, ApJ, 826, 87
Weisskopf, M. C., Elsner, R. C., Darbro, W., et al. 1984, ApJ, 278, 711
White, N. E., Mason, K. O., & Sanford, P. W. 1977, Natur, 267, 229
Williams, B. F., Durbin, M. J., Dalcanton, J. J., et al. 2021, ApJS, 253, 53
Wizinowich, P., Acton, D. S., Shelton, C., et al. 2000, PASP, 112, 315
Wolszczan, A., & Frail, D. A. 1992, Natur, 355, 145
Wood, K. S., Meekins, J. F., Yentis, D. J., et al. 1984, ApJS, 56, 507
Wright, E. L., Eisenhardt, P. R. M., Mainzer, A. K., et al. 2010, AJ, 140, 1868
Yatabe, F., Makishima, K., Mihara, T., et al. 2018, PASJ, 70, 89
Zhao, Y., Gandhi, P., Dashwood Brown, C., et al. 2023, MNRAS, 525, 1498
Zorec, J., Frémat, Y., & Cidale, L. 2005, A&A, 441, 235
Zurita Heras, J. A., & Chaty, S. 2009, A&A, 493, L1